J. Fluid Mech. (2006), *vol.* 549, *pp.* 273–306.
doi:10.1017/S0022112005007962 Printed in the United Kingdom

Atomization by jet impact

By N. BREMOND AND E. VILLERMAUX†

IRPHE, Université de Provence, Aix–Marseille I, Technopôle de Château-Gombert, 49, rue Frédéric Joliot-Curie 13384 Marseille Cedex 13, France

(Received 9 September 2004 and in revised form 8 July 2005)

The formation and fragmentation of liquid sheets resulting from the oblique collision of two identical cylindrical jets is investigated. The liquid expands radially from the impacting point forming a sheet in the form of a bay leaf bounded by a thicker rim. The sheet shape, rim size and liquid velocity field are quantified and represented analytically. External harmonic perturbations of the injection conditions reveal the nature of the rim destabilization and of its coupling with the sheet. Flow perturbations in the incident jets lead to sheet thickness modulations which trigger the fragmentation of the rim via the formation of liquid ligaments whose dynamics is described. The breakup of these ligaments induce both the shape and width of the drop size distribution in the spray formed by this process.

1. Introduction

The fragmentation of compact macroscopic objects is a typical phenomenon bridging complicated microscopic phenomena, such as fracture in solid comminution and breakup in liquid atomization, with non-trivial, and often broad statistics, namely that of the fragment sizes. As for liquid atomization, drops come from the rupture of objects having the form of threads or ligaments; the smooth, uniform long liquid cylinder has thus very soon become the paradigm of droplet formation. Following the early observation of Mariotte (1686) and Savart (1833*a–d*) that a liquid jet eventually ends in a train of droplets, subsequent studies have explained why the basic smooth state is unstable (Plateau 1873), how fast the instability develops (Rayleigh 1879) and how the thread finally disrupts into disjoined parcels (Eggers 1997), even in the presence of Brownian noise (Moseler & Landman 2000; Eggers 2002).

Yet, a phenomenon contingent to the formation of either natural or man-made sprays is the broad distribution of the drop sizes. Little is known about the reasons for this, although Villermaux, Marmottant & Duplat (2004) Marmottant & Villermaux (2004*a*, *b*) have suggested, and provided some experimental evidence, that a coalescence-like effect within the ligaments themselves while they break is responsible for the size polydispersity of the resulting spray. One of the reasons for the lack of detailed knowledge of this aspect of spray formation – although crucial for both industrial (Lefebvre 1989; Bayvel & Orzechowski 1993; Yang & Anderson 1995) and geophysical (Mason 1971; Seinfeld & Pandis 1998) applications – is the difficulty of devising an experimental set-up with control parameters influencing appreciably, and over a substantial range, the quality of atomization, that is the width of the drop size distribution. The present study is an attempt in this direction.

† Also at: Institut Universitaire de France.

An easy and widely used way to produce a spray is to form a liquid sheet by letting a jet impact on a solid surface, or on a facing similar jet. The sheet disintegrates into drops by the destabilization of its edges. The pioneer works of Savart (1833*a*–*b*), and later Taylor (1959*a*, *b*) and Huang (1970) essentially focused on the resulting sheet shape and its spatial extension. The quantitative study of the drop formation process itself was addressed only recently (Clanet & Villermaux 2002; Villermaux & Clanet 2002).

In the oblique collision of two identical jets, the axisymmetry of the facing configuration is lost. The liquid expands radially forming a sheet in the form of a bay leaf bounded by a thicker rim. The thickness of the sheet now depends not only on the distance from the collision point, but also on an angular coordinate (Taylor 1960). This thickness distribution was determined theoretically by Hasson & Peck (1964) assuming a top-hat velocity profile in the jets and a non-dissipative impact. Their prediction is in good agreement with the measurements of Miller (1960) and Taylor (1960). In these conditions, the liquid velocity in the sheet is expected to be constant and independent of the angular position. Choo & Kang (2002) have indeed measured a polar distribution of the liquid velocity owing to an initial developed velocity profile in the incident jets. A theoretical estimation of the thickness and velocity distributions for two incident jets with any given velocity profile different from a top hat is apparently lacking. Ibrahim & Przekwas (1991) suggest a semi-empirical expression of the sheet thickness distribution based on the experimental work of Naber & Reitz (1988), but assume a uniform jet velocity also. Bush & Hasha (2004) determine the sheet shape by measuring the dependence of the flow rate with the angular position.

Heidmann, Priem & Humphrey (1957) reported experimental observations on the spray formed by two impacting jets. They noted a first regime without drop formation, a second regime of periodic breakup of the sheet rim, and a fragmented regime at higher jet velocities for which the sheet is cut in periodic transverse strips. Dombrowski & Hooper (1963), Dombrowski & Neale (1974), Anderson, Ryan & Santoro (1995), Ryan *et al.* (1995) also observed the formation of transverse ligaments for turbulent, or vibrated impinging jets, and Bush & Hasha (2004) reported on a periodic fragmentation of the sheet occurring within a certain range of the impinging jet Reynolds and Weber numbers. These ligaments are reminiscent of those observed when the velocity contrast between the liquid surface and the ambient gas phase is large enough for a shear instability to develop (see e.g. Squire 1953; Mansour & Chigier 1990; Villermaux & Clanet 2002) which triggers a transverse Rayleigh–Taylor type of instability (Bremond 2003; Marmottant & Villermaux 2004*a*, *b*) leading to longitudinal ligaments, and drops.

In the present study, the jets are laminar, and the liquid velocity range is such that the interaction with the ambient quiescent air is negligible. The stable sheet thus obtained is bounded by a curved cylindrical rim, as seen in figure 2(*a*). The rim may therefore potentially suffer a capillary instability of a Plateau–Rayleigh type (Plateau 1873; Rayleigh 1879) because of its cylindrical cross-section, and a centrifugal Rayleigh–Taylor type of instability (Rayleigh 1883; Taylor 1950) because of the rim curvature. This instability is encountered in the rotating-cup configuration studied by Hinze & Milborn (1950) and Einsenklam (1964). Both instabilities have been considered by Clark & Dombrowski (1972) for a fan spray configuration and by Bush & Hasha (2004) for the impinging-jet case; these last authors dismiss the centrifugal instability based on an observation of the most unstable wavelength of the rim.

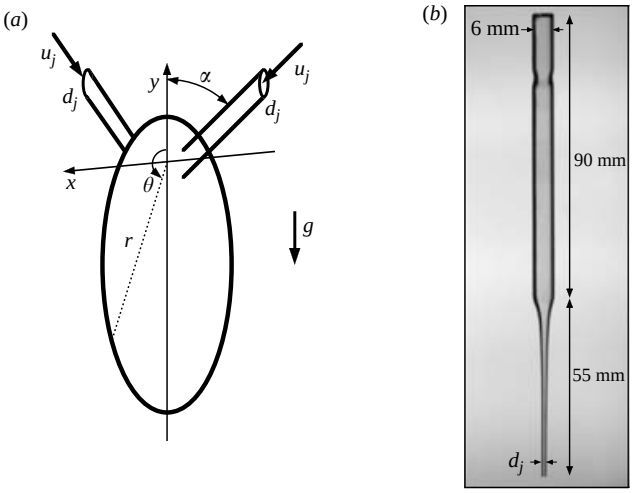

FIGURE 1. (*a*) Collision parameters of the coordinates and jets. (*b*) Pasteur pipette used as injector.

The aim of the present work is to examine the processes of the sheet destabilization (§§3 and 4), in order to give a quantitative description of the overall drop size distribution in terms of the dynamics of the objects (§5) involved in the fragmentation process (§6). Finally, the effect of the initial jet velocity profile on the sheet speed and thickness fields is discussed (Appendix A).

2. Experimental set-up

The liquid sheets are formed by the collision of two identical jets impacting at an angle 2α. A schematic of the jet impact configuration is presented in figure 1(*a*). The impact angle 2α varies from 58° to 117°. Pasteur pipettes shown in figure 1(*b*) are used as injectors. The pipette is a 6 mm inner diameter glass cylinder stretched at one of its extremities to form a convergent ending with diameter d_j. The convergence allows a smooth contraction of the liquid streamlines. We used two different injector diameters d_j of 1.05 mm and 1.42 mm. The liquid jet diameters are set by the injector diameters and the impacting distance is about three times d_j. The jet velocity u_j is measured from the mass flow rate through each injector with a high-precision balance (Sartorius LA6200S, $\Delta m = 0.01$ g) and a stopwatch. The jet velocity was between 1.5 and 4.6 m s^{-1}. Working fluids are water (density $\rho = 1000\,\mathrm{kg\,m^{-3}}$, surface tension $\sigma = 0.073\,\mathrm{kg\,s^{-2}}$) and ethanol (density $\rho = 810\,\mathrm{kg\,m^{-3}}$, surface tension $\sigma = 0.022\,\mathrm{kg\,s^{-2}}$). From *CRC Handbook of Chemistry and Physics*, the kinematic viscosity ν of ethanol at 20°C is $1.52 \times 10^{-6}\,\mathrm{m^2\,s^{-1}}$, slightly larger than that of water for which $\nu = 10^{-6}\,\mathrm{m^2\,s^{-1}}$.

All of our diagnostics are based on quantitative image analysis, resolved in both space and time. The time-resolved movies of the sheet instability dynamics were recorded by a Phantom V5 high-speed video camera. The white light source is a HMI projector (LTM of 575 W) operating by back lighting through a diffusing screen. The drop size measurements have been made from a collection of frozen images of the spray obtained by a back lighting 5 µs flash lamp triggered by a Hamamatsu

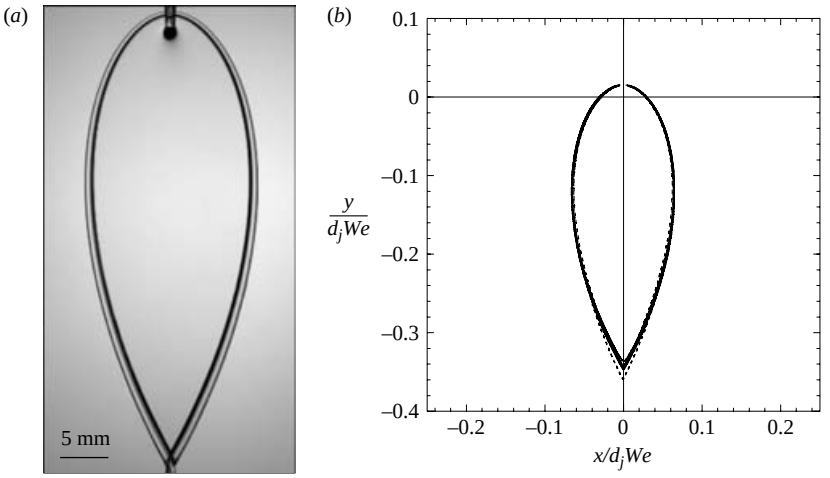

FIGURE 2. (*a*) Smooth ethanol sheet ($d_j = 1.05$ mm, $u_j = 1.8\,\mathrm{m\,s^{-1}}$ and $2\alpha = 89°$). (*b*) Experimental sheet contours normalized by the jet diameter d_j multiplied by the jet Weber number We for $2\alpha = 89°$, $d_j = 1.05$ mm (continuous line), and $d_j = 1.42$ mm (dotted line). We is varied between 75 and 305.

ORCA 1280×1024 pixels CCD array. The image-processing technique was originally described in Marmottant (2001) and Marmottant & Villermaux (2004*a*, *b*). An argon-ion laser in mono-mode at 488 nm was used for the interferometric measurements.

The jet Reynolds number $Re = u_j d_j/\nu$ varied between 900 and 4800, indicating that perturbations in the flow can be present naturally. The shape of the injector allows a smooth streamline contraction which flattens the velocity profile and delays the transition to a turbulent regime. The jet Weber number, $We = \rho u_j^2 d_j/\sigma$ was always larger than 50. It will be shown that the typical sheet size L varies as $d_j We$. The Froude numbers defined as $Fr = (gL/u_j^2)^{1/2}$ where g is the acceleration due to gravity, amount to the Bond number $Bo = d_j/l_c$ where $l_c = (\sigma/\rho g)^{1/2}$ is the capillary length. The Bond number, was always smaller than unity for all the experimental conditions and therefore gravity effects were neglected.

3. Basic state

3.1. *Observations*

Figure 2(*a*) is a front view of an ethanol sheet. The two jets collide forming a smooth sheet in the jet median plane bounded by a rim collecting the radially expanding liquid. The liquid flows into the rims on both sides of the sheet towards its tip where they impinge and eventually form another sheet in the perpendicular plane.

The sheet size depends on the collision conditions $\{u_j, d_j, \alpha\}$. As is customary in this class of problems involving an equilibrium between inertia and capillarity, the stationary shape displays a Weber number similarity (Taylor 1959*b*; Huang 1970; Clanet & Villermaux 2002). Figure 2(*b*) presents experimental contours normalized by $d_j We$ for several Weber numbers, the impact angle is set to $2\alpha = 89°$. As expected, all the contours collapse in a unique shape. As mentioned in §2, the ratio of the gravity to the inertia effects is given by the value of the Bond number $Bo = d_j/l_c$, where $l_c = (\sigma/\rho g)^{1/2}$ is the capillary length. A jet size increase of 35 % does not affect

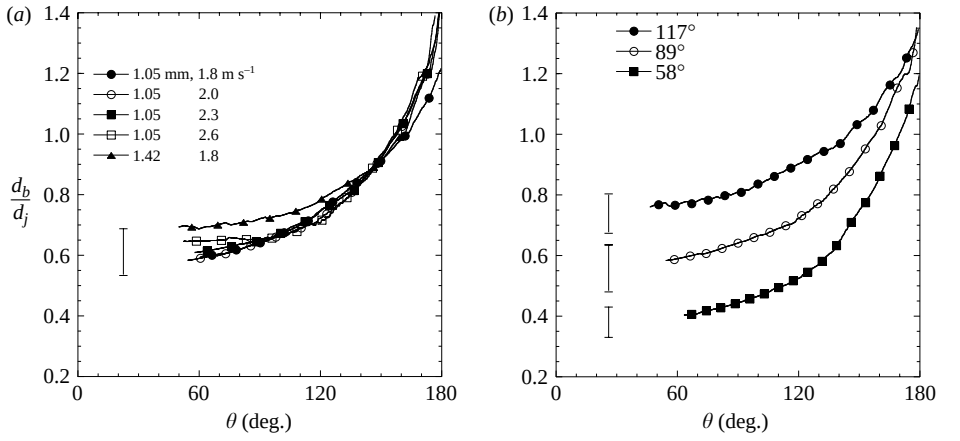

FIGURE 3. (*a*) Evolution of the rim diameter with the angular position for different jets properties, $2\alpha = 89°$. (*b*) Evolution of the rim diameter with the angular position for three impact angles 2α : ●, 117°; ○, 89°; ■, 58°. The jet diameter is equal to 1.05 mm and the jet velocity is, respectively, 1.8, 2.0 and 2.3 m s^{-1}. The vertical lines are the measurement error bars for each case.

the scaled sheet shape thereby confirming the negligible role played by gravity in the present conditions.

As seen in figure 2(*a*), the rim diameter d_b is an increasing function of the angular position θ. Figure 3 presents measurements of d_b for several collision conditions. The influence of the jet diameter and of the jet velocity is reported in figure 3(*a*), and the effect of the impact angle is shown in figure 3(*b*) where the rim size is normalized by the jet diameter d_j. The rim diameter is independent of the jet velocity and is proportional to the jet diameter (figure 3*a*). It becomes larger when the collision angle increases, as shown in figure 3(*b*).

As will be seen in the following sections, these features must be understood and modelled properly since they have a strong bearing on the resulting rim stability and atomization quality of this process.

3.2. *Shape*

In determining the sheet shape and rim characteristics, we follow the analysis of Taylor (1959*a*, *b*) on cusps bounding an axisymmetric sheet. The system of coordinates is presented in figure 4(*a*). The sheet speed is denoted by u and its thickness by h. The angle ϕ corresponds to the angle between the direction of a radius r and that of the rim tangent at the curvilinear abscissa s which is equal to zero for $\theta = 0$. The geometric relationship between these quantities is

$$\sin\phi = \frac{r\,\mathrm{d}\theta}{\mathrm{d}s}, \quad \tan\phi = \frac{r\,\mathrm{d}\theta}{\mathrm{d}r}. \tag{3.1}$$

The rim cross-section s_b, its velocity u_b and its radial position r are fixed by mass and momentum conservation. The aperture angle of a rim portion is equal to $\mathrm{d}\theta$ (figure 4*b*). Mass conservation in this rim portion is written as

$$\rho\frac{\mathrm{d}(u_b s_b)}{\mathrm{d}s} = \rho u \sin\phi h. \tag{3.2}$$

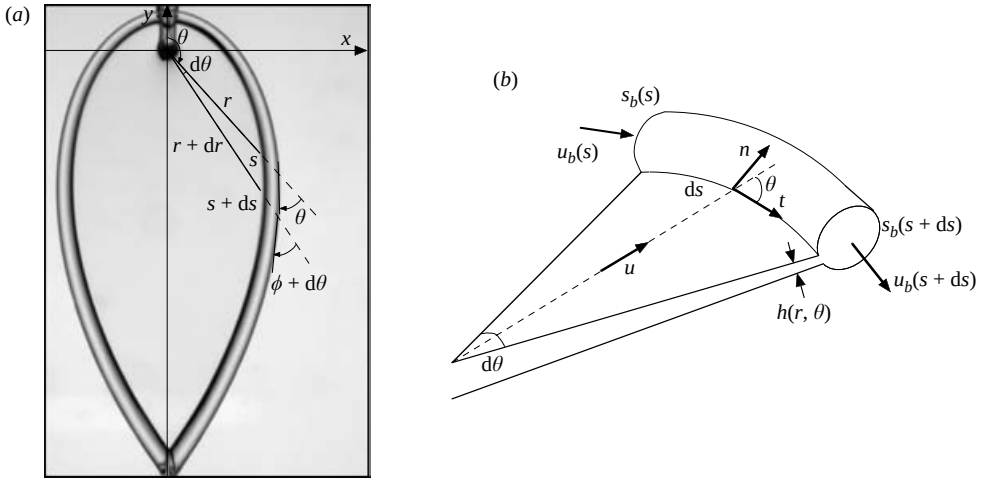

FIGURE 4. (*a*) Coordinate systems. (*b*) Control volume used for the mass and momentum conservation balances.

Similarly, the conservation of momentum tangential to the rim is given by

$$\rho \frac{\mathrm{d}\left(u_b^2 s_b\right)}{\mathrm{d}s} = \rho u^2 \sin\phi \cos\phi h, \tag{3.3}$$

and the conservation of momentum normal to the rim is

$$\rho u_b^2 s_b(\mathrm{d}\theta + \mathrm{d}\phi) = 2\sigma\, \mathrm{d}s - \rho u^2 \sin^2\phi h\, \mathrm{d}s. \tag{3.4}$$

The left-hand side of equation (3.4) corresponds to the centrifugal force imparted to the fluid particles because of the rim curvature. The first term of the right-hand side in equation (3.4) is the capillary force pulling back the rim and acting against the inertia injected into the rim represented by the second term.

The sheet thickness h depends on r, θ and α. Assuming a uniform top-hat velocity profile at the exit of the incident jets, and also an elastic non-dissipative impact, Hasson & Peck (1964) have shown that the sheet velocity remains equal to the jet velocity u_j and that the thickness distribution is given by

$$\frac{h}{d_j} = \frac{d_j}{4r} \frac{\sin^3\alpha}{(1 + \cos\theta\cos\alpha)^2}, \qquad u = u_j. \tag{3.5}$$

The effect of a jet parabolic velocity profile on the sheet features is discussed in Appendix A. We use d_j as the length scale and d_j/u_j as the time scale and denote the dimensionless quantities by a tilde. Using the geometric relationship $\mathrm{d}s = r\,\mathrm{d}\theta/\sin\phi$, the system of equations to solve providing the sheet and rim shape is

$$\frac{\mathrm{d}(\tilde{u}_b \tilde{s}_b)}{\mathrm{d}\theta} = F(\theta, \alpha), \tag{3.6a}$$

$$\frac{\mathrm{d}\left(\tilde{u}_b^2 \tilde{s}_b\right)}{\mathrm{d}\theta} = \cos\phi\ F(\theta, \alpha), \tag{3.6b}$$

$$\tilde{u}_b^2 \tilde{s}_b \left(1 + \frac{\mathrm{d}\phi}{\mathrm{d}\theta}\right) \sin\phi = \frac{2\tilde{r}}{We} - \sin^2\phi\ F(\theta, \alpha), \tag{3.6c}$$

$$\frac{\mathrm{d}\tilde{r}}{\tilde{r}} = \frac{\mathrm{d}\theta}{\tan\phi}, \tag{3.6d}$$

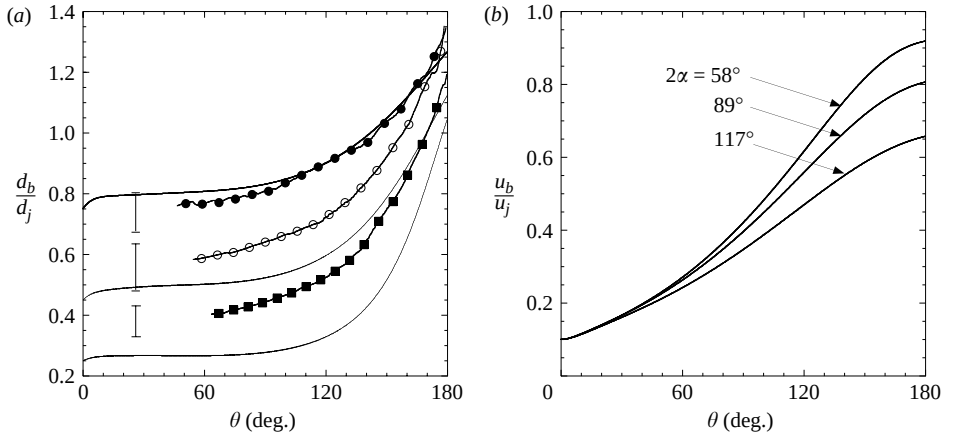

FIGURE 5. (*a*) Comparison between the experimental and predicted rim diameter for ●, $2\alpha = 117°$; ○, 89°; ■, 58°. (*b*) Rim velocity as a function of θ for the same collision conditions as in (*a*).

where $We = \rho d_j u_j^2/\sigma$ is the jet Weber number, and $F(\theta, \alpha) = hr = \sin^3\alpha/4(1 + \cos\alpha\cos\theta)^2$. Yarin (1993) provides a general formulation of the conservation laws at the level of the stress tensors involved, including viscoelastic effects, considers a radial flow in the sheet, but ignores the angular dependence of the thickness distribution of Hasson & Peck (1964). The above system has no simple analytical solution; however, this causes no great difficulty for the present discussion since (3.6*c*) clearly shows that distances scale as $d_j We$, and that, therefore, so does the size of the sheet, consistent with the observation of figure 2(*b*). We solve the system (3.6) numerically with initial conditions defined at $\theta = 0$ where the initial position of the rim $\tilde{r} = \tilde{r}_0(1-\epsilon)$ is moved back slightly ($\epsilon = 0.01$) from the stagnation-point location $\tilde{r}_0 = We\sin^3\alpha[8(1+\cos\alpha)^2]$, with $\phi = \arcsin(\sqrt{1-\epsilon})$ and $\tilde{u}_b = \cos\phi = \sqrt{\epsilon}$. The initial rim section $\tilde{s}_b$ is estimated from the experimental data shown in figure 3(*b*).

The evolution of the rim diameter with angular position predicted by (3.6) is presented in figure 5(*a*) together with the experimental data for several collision angles. The plateau for low angular position and then the increase of $\tilde{d}_b$ for larger θ is represented well by the model for $2\alpha = 117°$, but an increasing discrepancy appears when the collision angle decreases. The predicted evolution of the rim velocity is shown in figure 5(*b*) for the same collision angles. This velocity displays a steeper increase with θ for lower α.

A comparison between experimental and theoretical sheet shapes is displayed in figure 6(*a*) for the three impact angles. The contour is fairly well predicted by (3.6) assuming a uniform jet velocity profile at the exit, consistent with Hasson & Peck. We show in Appendix A how the result is altered when the velocity profile in the jets is of a Poiseuille type.

In the small impact angle α limit, the scaling laws for the sheet length L and maximal width W displayed in figure 6(*b*) can be understood as follows: for small α, the sheet length is essentially dominated by the distance between the impact point and the downstream tip. We anticipate that this distance is that travelled in the fluid particles in the sheet at velocity u_j in the time it takes for the rim to recess in the lateral direction by a distance W at a velocity whose order of magnitude is given by $\sqrt{\sigma/\rho h}$, the thickness h being the sheet thickness at the maximal extension L provided

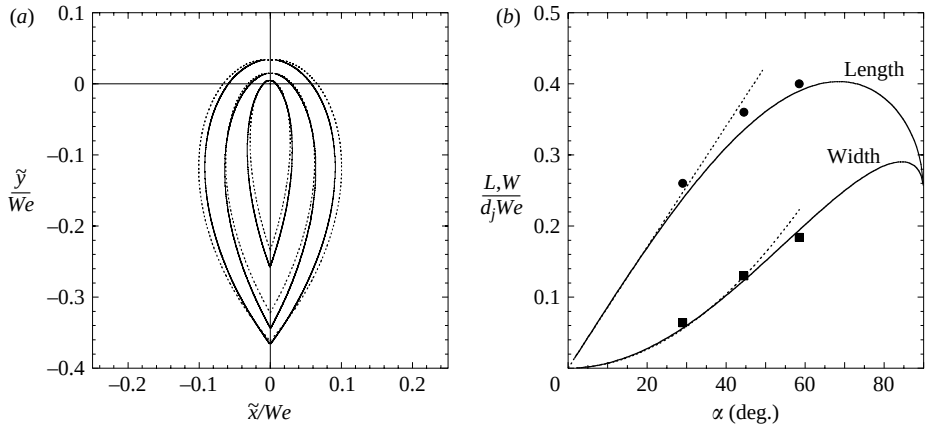

FIGURE 6. (*a*) Non-dimensional experimental sheet contours (continuous line) normalized by the jet Weber number *We* compared with the theoretical shape (dotted line) for $2\alpha = 58°$, $89°$ and $117°$, respectively, from the centre. (*b*) Total length L and maximal width W of the sheet normalized by *We* as a function of the impact angle α as predicted by equation (3.6), and experimental observations. The dotted lines show the trends $L/d_j We \sim \alpha$ and $W/d_j We \sim \alpha^2$, valid for small α.

by (3.5), that is $h \sim d_j^2/\alpha L$. We therefore have

$$L \sim u_j t^* \quad \text{with} \quad t^* \sim \frac{W}{\sqrt{\sigma/\rho h}}. \tag{3.7}$$

The impulse injected in the sheet perpendicular to its plane is of order $\rho(u_j \sin\alpha)^2 d_j^2 \approx \rho u_j \alpha^2 d_j^2$, and the typical width W is such that it equilibrates this impulse with surface tension, thus $W \sim \alpha^2 d_j We$. We finally anticipate that

$$L/d_j We \sim \alpha, \quad W/d_j We \sim \alpha^2, \tag{3.8}$$

consistent with the trends shown in figure 6(*b*).

It is also possible to estimate the critical Weber number below which no sheet can be formed. The rear extension of the sheet in $\theta = 0$ is $L_{rear} = d_j We(\sin\alpha)^3/(1+\cos\alpha)^2/8$. Half of the length of the major axis of the ellipse formed by the section of the cylindrical jet by the plane at an angle α is $dj/(2\sin\alpha)$ and its focus lies at $d_j/(2\tan\alpha)$ off the jet centre (Hasson & Peck 1964). L_{rear}/d_j must thus be larger than $(1/\sin\alpha - 1/\tan\alpha)/2$, providing a critical Weber number equal to $We_c = 4(1+\cos\alpha)/(\sin\alpha)^2$. It is equal to 4 for facing jets, and tends towards $8/\alpha^2$ for small α.

An additional observation is worth reporting: figure 7(*a*) is a snapshot of the liquid sheet when lit by reflection, revealing a pattern of curved lines starting from the top of the sheet, crossing and reflecting at the rim. This is a standing antisymmetrical (sinuous) wave of the same type as the cardioids observed by Taylor (1959*a*) on a circular liquid sheet. The velocity of this type of wave (Taylor 1959*a*) is $c = (2\sigma/\rho h)^{1/2}$. This is also the velocity of a liquid edge recessing under capillary forces (Taylor 1959*b*; Culick 1960) and the present dynamics accounts for these waves, when the centrifugal forces are suppressed, as if the rim was not curved, or as if the mass it carries did not contribute to its centrifugation. This is realized in our framework by letting the centrifugal term in equation (3.4) be zero. The angle ϕ between a streamline and the

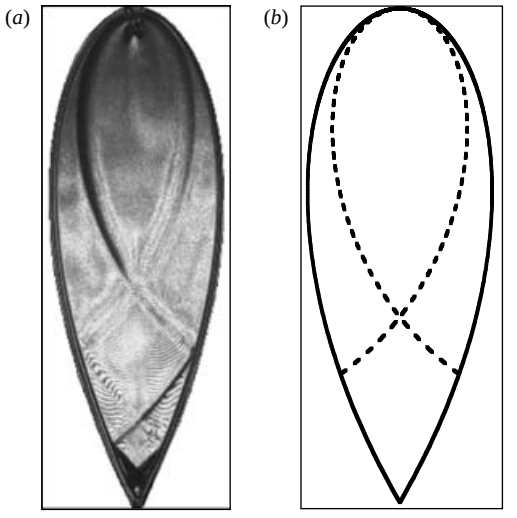

FIGURE 7. (*a*) Experimental observation of antisymmetrical waves on the sheet. (*b*) Calculated antisymmetrical waves pattern (dotted line).

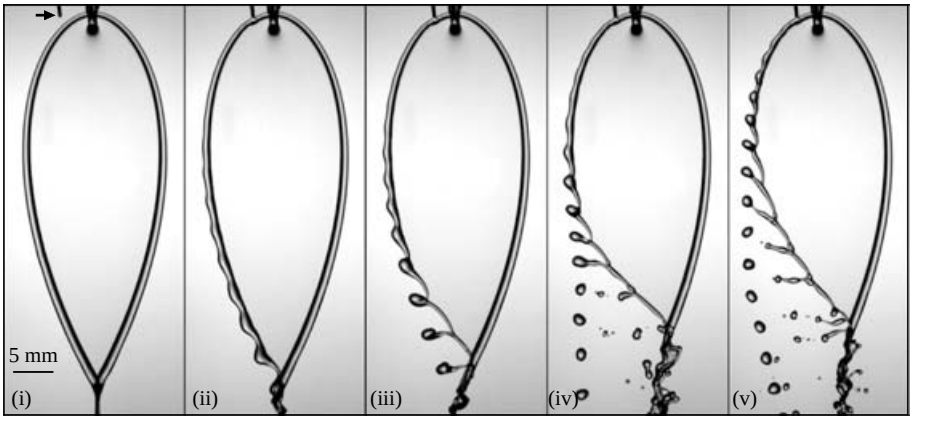

FIGURE 8. Perturbation with a small wire (indicated by an arrow) of an ethanol sheet rim with increasing levels of perturbation from left to right. The injection conditions are identical for each picture, $2\alpha = 90°$, $d_j = 1.05\,\mathrm{mm}$, $u_j = 1.7\,\mathrm{m\,s^{-1}}$.

tangent 'non-centrifuged rim' is then

$$\sin\phi = \frac{2\sigma}{\rho h\, u_j^2} = \frac{c^2}{u_j^2}. \tag{3.9}$$

This angle ϕ is simply the Mach angle between the antisymmetrical wave propagating direction and the direction of the flow. The position of the wave is determined by equations (3.1) and (3.9) and is plotted in figure 7(*b*) for a perturbation localized at $\theta = 0$. The position of the actual rim is also shown. It is now obvious that when the actual rim destabilizes and fragments, shedding mass in the form of drops, its position will lie in-between the two extreme positions, that of the rim without mass loss, and that of the rim without centrifugal inertia, as illustrated in figure 8.

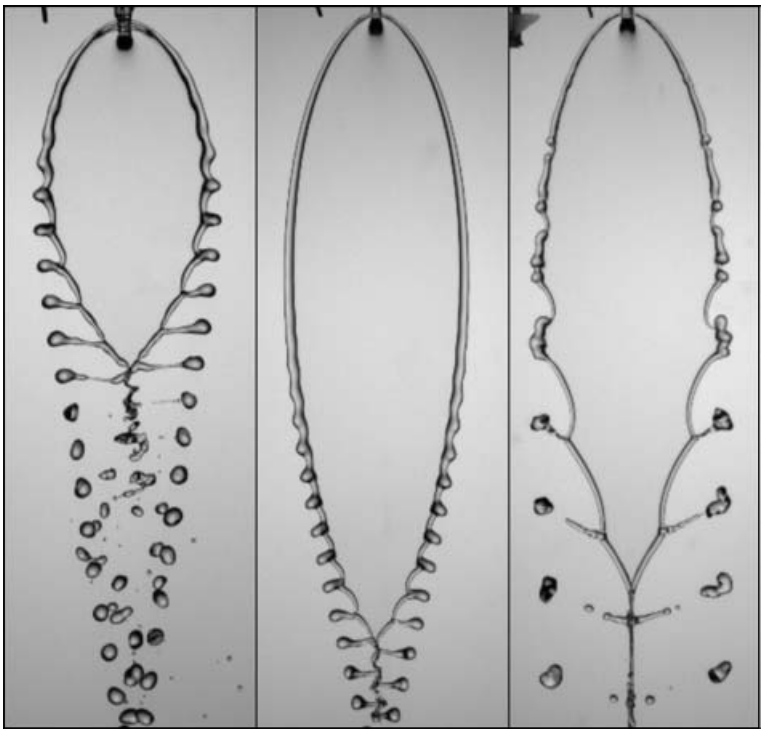

FIGURE 9. Periodic atomization of ethanol sheets.

4. Nature of the rim destabilization

4.1. *Phenomenology*

The smooth basic state obtained with ethanol is now perturbed. A tungsten wire of 400 μm diameter is brought towards the rim until it contacts the liquid. The wire is indicated with a black arrow on the first picture of figure 8. These pictures are snapshots taken at random. The rim disturbances grow with θ and eventually lead to the formation of a ligament connected to the sheet which breaks into smaller drops. This periodic process is accompanied by a retraction of the free edge between the ligaments. Note that the frequency of the destabilization is similar in each picture; it also remains constant when the jet velocity is varied and is roughly equal to 850 Hz. This frequency is not a signature of the wire wake in the rim since the use of a 200 μm wire in diameter did not change the atomization frequency.

It is also possible to realize a periodic atomization on both sides of the sheet, in a more or less symmetrical way, as shown in figure 9. This feature is similar to the observations reported by Heidmann *et al.* (1957) Dombrowski & Hooper (1963), Dombrowski & Neale (1974), Anderson *et al.* (1995), Ryan *et al.* (1995) and Bush & Hasha (2004). This configuration is obtained when a slight velocity contrast exists between the incident jets of the order of 10 cm s^{-1}. In this case, the sheet is no longer formed in the median plane of the jets, but slightly tilted. As a consequence, probably owing to the onset of a shear instability within the sheet associated to the initial velocity contrast, the rim is not smooth and the perturbations are convected on both sides of the sheet. The ensuing sheet fragmentation is still periodic, but not necessary strictly symmetric, as shown in figure 9.

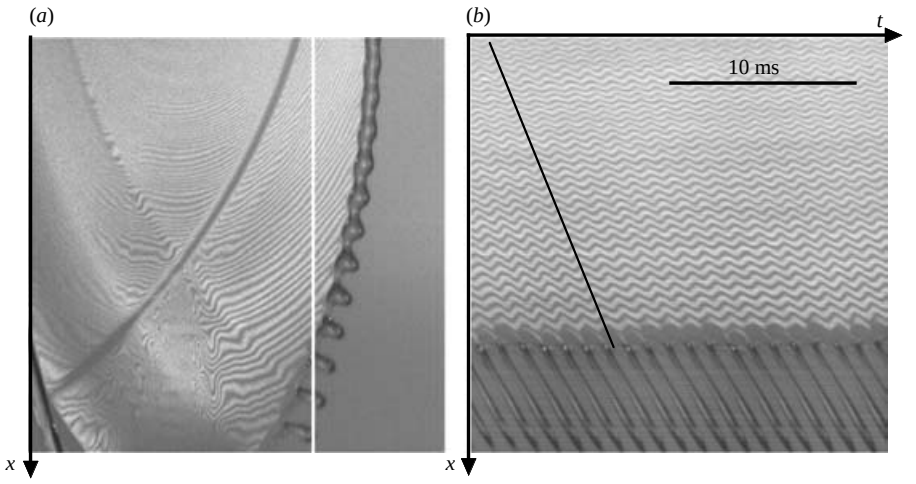

FIGURE 10. (*a*) Snapshot of the sheet thickness field revealed by laser interferometry. The rim is perturbed by a wire upstream. (*b*) Spatiotemporal diagram built with a vertical line selected on a set of pictures like (*a*). The selected line is shown in white on (*a*).

This last observation demonstrates that some information is transmitted from the impingement region towards the rim via the sheet itself. We therefore investigated the thickness modulations of the sheet through the interference pattern of an incident laser light. An example is shown in figure 10(*a*). The sheet is lit with an argon laser of wavelength 488 nm through a diffuser screen in a set-up similar to that of Dombrowski, Hasson & Ward (1960). The sheet is, in addition, back-lit with white light allowing the visualization of the rim.

Each fringe corresponds to a given value of the sheet thickness. Between two dark or bright fringes, the thickness variation Δh depends on the laser wavelength λ_L, on the incident angle i of the laser with the normal of the sheet and on the optical index n, as $\Delta h = \lambda_L/2n\cos i'$, where $\sin i = n \sin i'$. The distance between two fringes increases with radial position r owing to the thinning of the sheet with distance from the impacting point, and the fringes are curved because of the angular distribution of the thickness (see § 3.2).

Figure 10(*b*) is a spatiotemporal diagram built with a set of consecutive frames as shown in figure 10(*a*). The same vertical line is selected on each image and this sequence of lines forms a new picture where time goes from left to right. We note that all the fringes oscillate at the same frequency, but with a phase interval between two adjacent fringes pointing out the propagation of a thickness wave. The frequency of the thickness variation corresponds to the constant atomization frequency. The propagation of the wave is indicated by the black line in figure 10(*b*), and the wave velocity is constant. Figure 11 presents a temporal sequence of a close-up of the sheet seeded with a single small solid particle, indicated by a black point. The modulations of the thickness field propagate with a velocity equal to the particle velocity and therefore equal to the fluid velocity. This is consistent with the group velocity of this varicose long wave (compared to the sheet thickness) being much smaller than the advecting fluid velocity (e.g. Taylor 1959*a*). Note the constancy of the fluid flow in the sheet along a radius as observed by Choo & Kang (2002) and Bush & Hasha (2004).

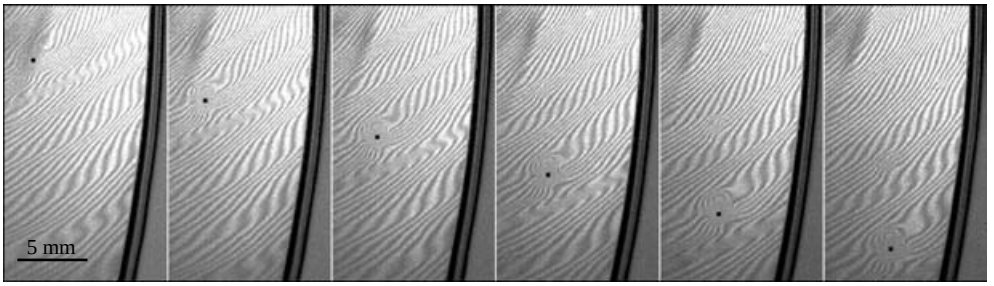

FIGURE 11. Solid particle convected by the flow showing the equality between the velocities of the fluid and of the thickness modulations. Time goes from left to right with a time step of 0.83 ms, $u_j = 2.4\,\mathrm{m\,s^{-1}}$.

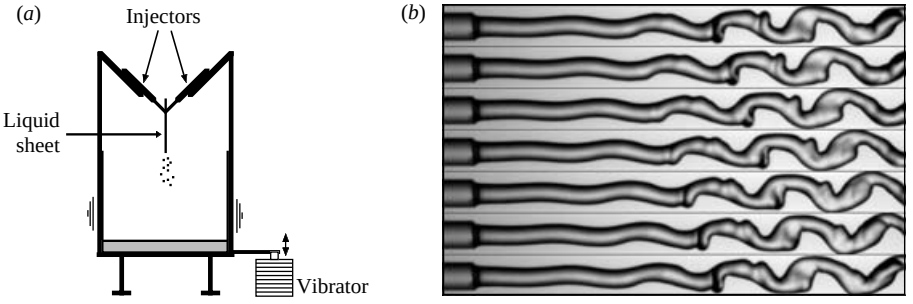

FIGURE 12. (*a*) Vibration of the experimental structure at a given frequency with the help of a vibrator. (*b*) Oscillation of one incident jet when the structure is vibrated at about 800 Hz.

To further illustrate the coupling between the sheet thickness modulations and the rim destabilization, we have introduced an external perturbation with a controlled frequency. As sketched in figure 12(*a*), a vibrator is connected to the base of the experimental structure. The imposed vibrations trigger velocity and impact angle fluctuations of the injectors at the forcing frequency, and an example of the resulting jet oscillation is shown in figure 12(*b*). The sheet thickness depends on the angle collision, (3.5), and this angle is modulated because of the injector oscillations. This effect is thus responsible for the formation of radial variations of the sheet thickness. The set-up supporting the experiment has a natural resonance frequency of about 800 Hz, explaining the periodic thickness modulations close to this frequency observed in figure 10(*b*) without external forcing.

The consequences of this external excitation on the sheet thickness are shown in figure 13 for different forcing frequencies. The modulations of the interference patterns reveal the thickness wave propagation, and the wave frequency is set by the forcing.

As shown in figure 13, a periodic atomization of the rim is achieved for frequencies between 600 Hz and 1000 Hz. The wavelength λ of the rim modulations increases or decreases when the frequency increases or decreases from this optimum ($\lambda \sim u_j/f$), and the destabilization is then slower. The optimum is reached for exciting frequencies corresponding to a spatial wavelength λ of the order of the rim diameter which make the rim instability similar to the familiar capillary instability of jets and threads, a point that we shall return to in the next section.

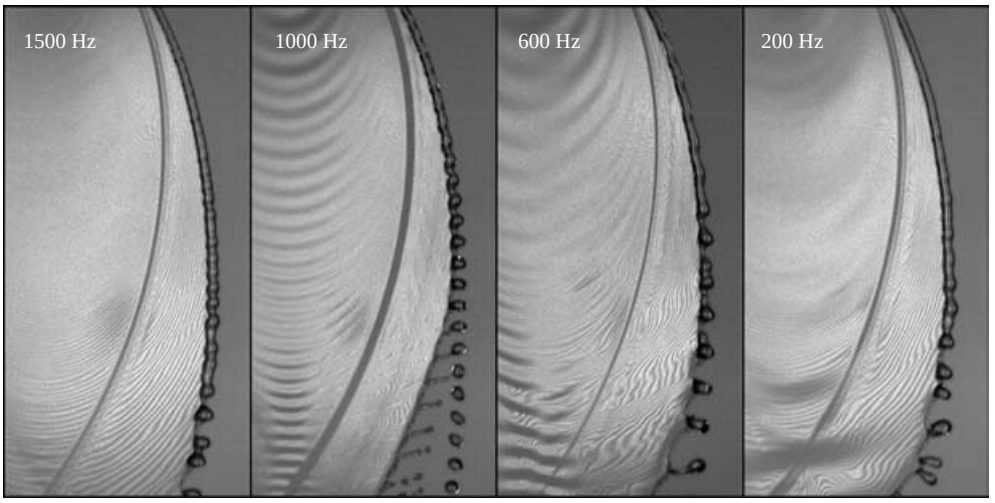

FIGURE 13. Effect of vibrations of the experimental structure on the thickness field and rim destabilization for different excitation frequencies, $d_j = 1.05\,\mathrm{mm}$, $u_j = 3.5\,\mathrm{m\,s^{-1}}$, $2\alpha = 90^\circ$.

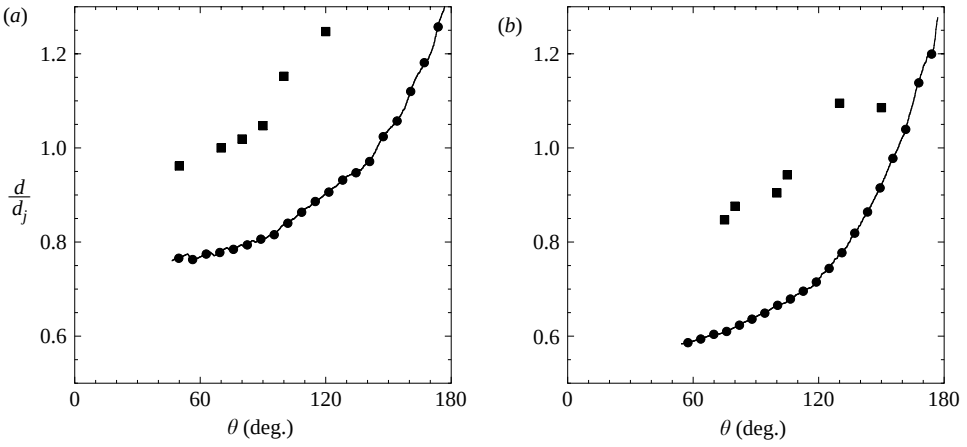

FIGURE 14. Correspondence between ●, the rim diameter and ■, the mean drops size plotted versus the corresponding ejection angle, (*a*) $2\alpha = 117^\circ$, (*b*) $2\alpha = 88^\circ$.

When the excitation is optimum, roughly one drop is formed per wavelength and therefore, by volume conservation, the drops size is $d \sim (\lambda d_b^2)^{1/3}$. Since $\lambda \sim d_b$, the drop size in that case is thus proportional to the local rim diameter. This is clearly apparent from figure 14 which presents the evolution with θ of the experimental rim diameter and of the mean drops size for different ejection angles obtained with water. On average, the mean drop size is 1.2 times larger than the local rim diameter at the angle of ejection.

We finally note in figure 13 that another type of wave is excited. These waves, manifested by an alternation of bright and dark curved strips, propagate towards the free edge with a constant passage frequency equal to the exciting frequency. These waves correspond to a sinuous mode for which both interfaces of the sheet oscillate in phase (Taylor 1959*a*). The laser light in then deflected because of the tilted liquid surface, inducing the formation of dark strips.

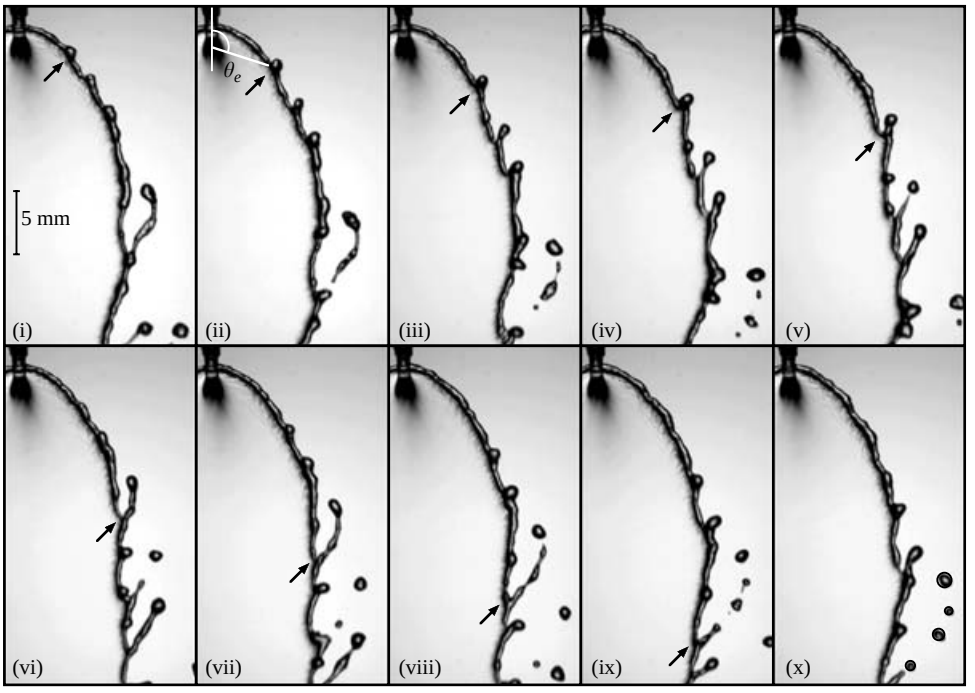

FIGURE 15. Time evolution of the rim destabilization, ligament formation and stretching, and then drops formation at the edge of a water sheet, $d_j = 1.05\,\mathrm{mm}$, $u_j = 3.5\,\mathrm{m\,s^{-1}}$, $2\alpha = 72^\circ$. The time step is 1 ms.

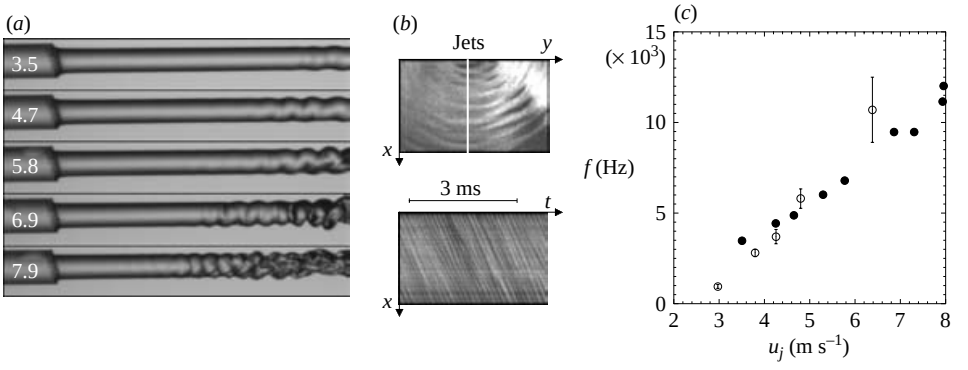

FIGURE 16. (*a*) Shear instability development on a water jet for several jet velocities as indicated on the injector in $\mathrm{m\,s^{-1}}$, $d_j = 1.05\,\mathrm{mm}$. (*b*) Close-up view of the sheet near the jet impact location showing surface waves, and the corresponding spatiotemporal diagram built with a vertical line marked in white, $u_j = 6.4\,\mathrm{m\,s^{-1}}$, $2\alpha = 90^\circ$. (*c*) Frequencies of ●, the jet waves and ○, the sheet waves as a function of the jet velocity.

4.2. *Lower viscosity liquid*

The jet Reynolds number was varied between 900 and 2400 in the previous experiments, involving ethanol as a working fluid. For the same range of operating Weber numbers, the jet Reynolds number is sensibly larger when using water, since Re is varied between 2100 and 4800. No stable state is observed in that case and the sheet is naturally perturbed, as can be seen in figure 15 because of disturbances coming from the injection jets themselves, as can be seen in figure 16(*a*). This figure

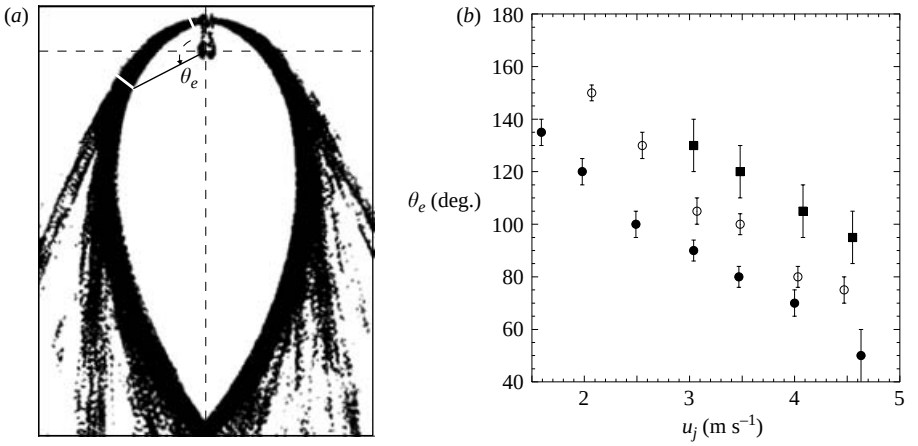

FIGURE 17. (*a*) Definition and measurement of the ejection angle θ_e. (*b*) Evolution of θ_e with jet velocity for three collision angles: ●, 117°; ○, 88°; ■, 72°.

also shows that the higher the jet velocity, the larger the disturbances, mainly in the form of a helical mode, characteristics of this intermediate Reynolds number range (Ho & Huerre 1984). The passage frequency f_p of the jet preferred mode modulations is reported in figure 16(*c*) as a function of the jet velocity. As indicated in §4.1, a perturbation of the injection induces the formation of sinuous and varicose waves on the sheet, with the same frequency, and this property is used to determine the frequency of the thickness modulation waves. A close view of the sheet near the jet impact is shown in figure 16(*b*), the sheet being lit by reflection. Some curved dark strips indicate the presence of surface waves. A spatiotemporal diagram built from a vertical line is also shown in figure 16(*b*). The propagation of a wave can be followed by the shadow created by the crest which forms oblique dark lines on the spatiotemporal diagram. The passage frequency of the waves measured from this diagram is reported in figure 16(*c*). This frequency is an increasing function of the jet velocity and is of the order of the preferred mode frequency of the jets. Thickness modulations are thus periodically injected in the liquid sheet. These waves reflect the state of the flow field in the incident jets via the shear instability development which depends on the exit boundary-layer features (Ho & Huerre 1984). For a fully developed flow, the Strouhal number of the jet, $f_p d_j/u_j$, is constant. To this temporal excitation of the rim corresponds a spatial wavelength which scales as d_j as well as the rim diameter. These waves were not observed for the lower-Reynolds-number experiments using ethanol without external forcing, explaining why the rim was not spontaneously destabilized in that case. These waves are similar to that observed by Dombrowski & Hooper (1963), working with higher jet speeds. This is further discussed in Appendix A.

The time evolution of the rim destabilization is shown in figure 15. Initially, small disturbances on the rim grow with θ, leading to the formation of a ligament which finally breaks up into several drops. Drops are detached from the sheet as soon as their trajectory differs from that of the rim contour. Then, the drops follow a ballistic trajectory which is initially straight owing to their ejection velocity being $> 1\,\mathrm{m\,s^{-1}}$. The future drop in figure 15 reaches a critical angle in picture (ii), after which its trajectory is a straight line. This angular position defines the ejection angle θ_e.

Figure 17(*a*) is the average of a temporal series of front views from the water sheet and the final picture is made binary. We note a straight envelope reflecting the

trajectories of the ejected drops. The black area around the sheet before θ_e represents the envelope of the amplifying rim disturbances. The thickness of the average envelope at θ_e, indicated by a white line in figure 17(*a*), is twice the initial rim size. That ratio holds for all the collision conditions we have studied. As seen in figure 17(*b*), the larger the collision angle, the smaller the ejection angle θ_e. The ejection angle decreases with increasing jet velocity, and is about 180° for low jet velocities, meaning that no drops are ejected in that limit. For lower velocities, however, no sheet is formed any more and the colliding jets coalesce into a single jet.

5. Rim instability

5.1. *Sheet-rim coupling*

The observations depicted above suggest that a capillary instability of a Plateau–Rayleigh type (Plateau 1873; Rayleigh 1879) is responsible for the rim destabilization. At least, the fact that the local rim diameter sets the instability wavelength is an insight in this direction. However, the sheet rim is an open system continuously fed by the liquid flowing in the sheet to which it is attached. Consequently, and by contrast with the classical capillary instability of a quiescent liquid ligament, the rim sustains a non-uniform, accelerated axial velocity.

We formulate the mass and momentum balances in the long-wave approximation (Weber 1931) and slender-slope approximation ($\partial_s r \ll 1$) in a local frame with u_b the axial velocity along the ligament and r_b its radius

$$\left.\begin{aligned} &\partial_t r_b^2 + \partial_s\left(u_b r_b^2\right) = \frac{Q}{\pi},\\ &\partial_t u_b + u_b \partial_s u_b = -\frac{1}{\rho}\partial_s p + M,\\ &p = \sigma\left(\frac{1}{r_b} - \partial_s^2 r_b\right),\\ &\text{with}\quad Q = h u_\perp,\ M = \frac{Q}{\pi r_b^2}(u_\parallel - u_b), \end{aligned}\right\} \tag{5.1}$$

where $u_\perp$ denotes the component of the liquid velocity in the sheet perpendicular to the rim, and $u_\parallel$ its component parallel to the rim at that location. The sheet thickness is denoted by h. The full Laplace pressure term,

$$p = \sigma\left(\frac{1}{r_b\left(1 + r_b'^2\right)^{1/2}} - \frac{r_b''}{\left(1 + r_b'^2\right)^{3/2}}\right). \tag{5.2}$$

coincides with that used in (5.1) when $r_b' = \partial_s r_b \ll 1$, precisely in the slender-slope limit.

The study of the basic state shows that the rim is nearly constant in radius for a portion of the arclength s along the basic state shape (for angles smaller than 120° to 140°), and that the axial velocity increases roughly linearly over the corresponding locations, as we can see from figure 5. This is, of course, an idealization of more complicated dependences in reality, but restricting the description to this simplified basic state allows us to examine the impact of a longitudinal stretch on the rim dynamics. We therefore express the basic state as $\{u_b, r_b\} = \{u_0 + \gamma s, r_0\}$ with r_0 independent of s. The steady-state solution of (5.1) is $\pi r_0^2 = q_0/\gamma$ and $u_0 = u_\parallel/2$ where q_0 is the steady contribution to the flow rate Q injected into the rim through the sheet. We decompose $Q = q_0 + q$ and $M = m_0 + m$ with $m_0 = \gamma u_\parallel/2$, where q and m are

the fluctuating parts of the flow rate and momentum injected in the rim, respectively, owing to fluctuations in h, $u_\perp$ and $u_\parallel$ whose temporal phases are left *a priori* free and decoupled. We thus investigate the stability of the above system by deriving the dynamics for small velocity and radius perturbations u and r, which reads

$$\left.\begin{aligned} &\partial_t r + u_0\partial_s r + \gamma r + \frac{r_0}{2}\partial_s u = \frac{q}{2r_0}, \\ &\partial_t u + u_0\partial_s u + \gamma u = -\frac{\sigma}{\rho}\left(-\frac{1}{r_0^2}\partial_s r - \partial_s^3 r\right) + m. \end{aligned}\right\} \tag{5.3}$$

The terms proportional to $u_0\partial_s$ in the above system reflect a trivial displacement at velocity u_0. We therefore study the dynamics for the radius modulations r in a reference frame travelling at velocity u_0 by making the transformation $r(s,t) \to r(s',t')$ with $s' = s - u_0 t$ and $t' = t$. Having thus eliminated the convection terms, we finally obtain

$$\partial_t^2 r + 2\gamma\partial_t r + \gamma^2 r - \frac{\sigma}{2\rho r_0^3}\left(-r_0^2\partial_{s'}^2 r - r_0^4\partial_{s'}^4 r\right) = \frac{1}{2r_0}(\partial_t q + \gamma q) - \frac{r_0}{2}\partial_{s'} m, \tag{5.4}$$

which describes the dynamics of the (possibly unstable) radius modulation waves along the sheet rim. This is the characteristic equation of an over-damped oscillator with a source term depending on the shape of the rim undulations via its spatial derivatives. The forcing terms on the right-hand side of (5.4) reflect the way the rim is fed by the liquid sheet. This generalizes the inviscid dynamics obtained for an isolated uniform liquid cylinder (Weber 1931) to a cylinder fed on its side by possibly time-dependent injection rates q and m.

Looking for solutions of the form $r = \xi(t)\mathrm{e}^{\mathrm{i}ks'}$ and rescaling time by $\sqrt{2\rho r_0^3/\sigma}$ and the wavenumbers by r_0, we obtain

$$\partial_t^2\xi + 2\gamma\partial_t\xi + \gamma^2\xi - (k^2\mathrm{e}^{-2\gamma t} - k^4 e^{-4\gamma t})\xi = f(k,t), \tag{5.5}$$

where $f(k,t)$ stands for the Fourier transform of the right-hand side of (5.4). The perturbations along the rim are transported by material particles; they are thus stretched by the base flow. Therefore, following Saffman (1974), stretching of the wavenumbers for which an initial k becomes $k\mathrm{e}^{-\gamma t}$ in the course of time, has been accounted for in obtaining (5.5).

Because of the capillary destabilizing term initially proportional to $k^2 - k^4$ arising from the circular geometry of the rim's cross-section, the dynamics of ξ in (5.5) may lead to an amplification, even in the absence of external noise, i.e. for $f(k,t) \equiv 0$. For a wavenumber k, lying in the initial unstable range ($k < 1$), the early time ($\gamma t \ll 1$) unstable branch for ξ is proportional to $\exp(-\gamma + \sqrt{k^2 - k^4})$ and leads to an amplification, provided the stretching rate is not too strong, that is, $\gamma < \sqrt{k^2 - k^4}$. The long time ($\gamma t \gg 1$) response of ξ in (5.5) is always dominated by stretching, and ξ decays as $\mathrm{e}^{-\gamma t}$, thereby trivially following the stretching-induced rate of approach of the marginal stability condition at $k = 0$. The initially (when $\gamma t \ll 1$) most amplified mode which results from the maximization of $k^2 - k^4$ is equal to $k_m = 1/\sqrt{2}$ in units of the rim radius. It is likely to be amplified if $\gamma < 1/2$.

5.2. *The stretching rate*

The stretching rate experienced by fluid particles in the rim is equal to, in dimensional units, $\mathrm{d}u_b/\mathrm{d}s$, where s is the curvilinear abscissa along the rim. The velocity in the rim u_b scales as the jet velocity u_j, and the sheet size L varies as $\alpha d_j We$ (see § 3); therefore, the stretching rate typically scales as $u_j/d_j \times (\alpha We)^{-1}$. As for the rim radius,

it remains of the order of the injection diameter d_j, as shown in figure 5. Since the capillary time based on the rim radius serves as the time of reference in (5.5), the scaled stretching rate γ is thus, in the impinging jet configuration, of the order of

$$\gamma \equiv \frac{u_j}{L} \simeq \frac{u_j}{\alpha d_j We}\sqrt{\frac{\rho d_j^3}{\sigma}} = \frac{1}{\alpha\sqrt{We}}. \tag{5.6}$$

Considering the practical values of the Weber number, typically of the order of several hundred, the above quantity is appreciably smaller than unity, indicating that the rate of stretch is not strong enough to overcome the capillary destabilization of the rim which, therefore, destabilizes in a time scale of the order of $\sqrt{\rho d_j^3/\sigma}$. Note that the same discussion as that leading to (5.6) shows that the ratio of the residence time of the perturbations along the rim, typically given by $d_j We/u_j$ to the capillary destabilization time is of the order of $We^{1/2}$. The instability has thus, in principle, time to grow.

This idealization of the rim dynamics explains why these sheets formed by jet impaction are 'fragile objects': they are sensitive to external perturbations, precisely because their border is linearly unstable. It is also clear now why the optimal perturbation described in § 4.1 is that giving rise to spatial disturbances in the sheet whose wavelength is of the order of the rim's radius; this characteristic scale is precisely the one which is most amplified by the capillary instability of the rim.

The role played by the noise in the dynamical equation (5.5) for the disturbances along the rim is transparent as well: if $f(k, t)$ has a peak around $k \simeq k_m \sim 1/d_b \simeq 1/d_j$, as in the present experiments involving disturbed jets, then the instability is excited at its optimal mode, and is therefore hastened. This effect concludes on the 'sheet–rim' coupling phenomenon in this system.

5.3. *Capillary versus centrifugal instability*

We have up to now left aside the effects associated with the natural curvature of the rim in its basic state. Because of this curvature, the particles running along the rim are subjected to an acceleration perpendicular to the sheet edge, and directed towards the liquid in the plane defined by the sheet. This situation is thus potentially unstable in the sense of Taylor (1950), following the early remark of Rayleigh (1883). This effect is dominant in the atomization process involving spinning disks and cups where the acceleration is communicated to the liquid by rotation and which destabilizes in a set of regularly spaced ligaments, as shown by Einsenklam (1964). In the present configuration, the liquid is subjected to a centrifugal acceleration g_c equal to u_b^2/R_c, where $R_c = \mathrm{d}s/(\mathrm{d}\theta + \mathrm{d}\phi)$ is the radius of curvature of the sheet free edge. Its order of magnitude is $d_j We$. The characteristic time of the development of the associated instability is $t_{RT} = (\sigma/\rho g_c^3)^{1/4}$. This instability may compete in the present system with the Plateau–Rayleigh capillary instability depicted above, whose characteristic time, constructed with the rim diameter is $t_{PR} = (\rho d_b^3/\sigma)^{1/2}$.

This question cannot be settled on dimensional grounds only, since both t_{RT} and t_{PR} have the same scaling dependencies, i.e. both are proportional to $d_j/u_j \times We^{1/2}$. Both mechanisms also anticipate the same most unstable wavelength since the capillary scale for the acceleration g_c given by $\sqrt{\sigma/\rho g_c}$ is proportional to d_j, itself proportional to d_b, as well. A detailed analysis of the relative absolute values of the amplifications associated to these two mechanisms is thus required.

Because the rim diameter and radius of curvature depend quantitatively on the angular position, the net gains of both instabilities accounting for these variations

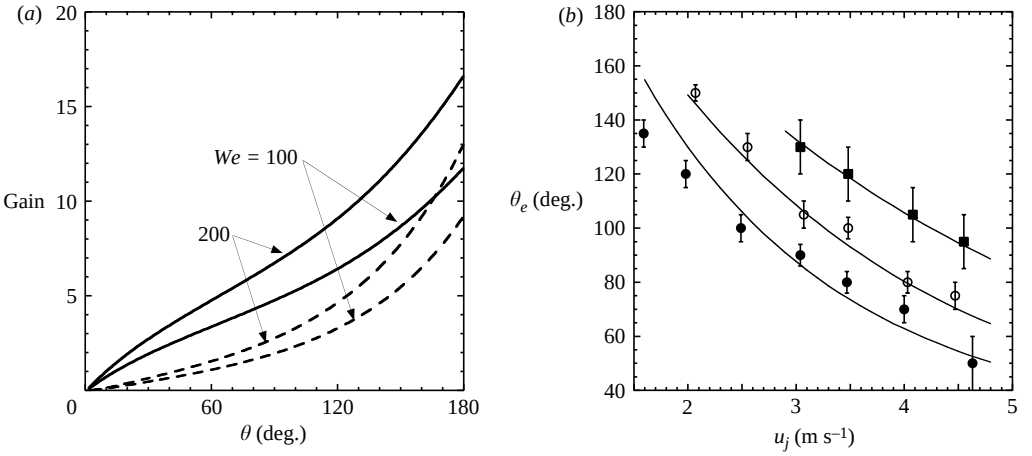

FIGURE 18. (*a*) Gains of the Plateau–Rayleigh instability (solid line) and of the Rayleigh–Taylor instability (dashed line) of the rim as a function of θ for two jet Weber numbers, 100 and 200, and $2\alpha = 90°$. (*b*) Prediction of the drop formation angle due to the capillary instability of the rim for a critical gain equal adjusted to 6, 6.5 and 7, respectively, for ●, $2\alpha = 117°$; ○, $2\alpha = 88°$; ■, $2\alpha = 72°$.

have to be computed in order to determine which one leads to the higher amplification. We simply estimate the gain G as the integration over the residence time of the particles of the local amplification rate given by the inverse of the characteristic instability time scales. Indeed, for both instabilities, the group velocity is zero and the perturbations grow while being convected by the flow. The dimensionless time of a fluid particle depends on angular position θ as

$$\tilde{t}(\theta) = \int_0^{\theta} \frac{\tilde{s}(\theta')}{\tilde{u}_b(\theta')}\,\mathrm{d}\theta', \tag{5.7}$$

and the gains of both instabilities are then

$$G_{RT}(\theta) = \int_0^{\theta} \frac{\tilde{s}(\theta')}{\tilde{t}_{RT}(\theta)\tilde{u}_b(\theta')}\,\mathrm{d}\theta', \quad G_{PR}(\theta) = \int_0^{\theta} \frac{\tilde{s}(\theta')}{\tilde{t}_{PR}(\theta)\tilde{u}_b(\theta')}\,\mathrm{d}\theta'. \tag{5.8}$$

Both gains are plotted in figure 18(*a*) versus the angular position along the rim θ, for two jet Weber numbers. The Plateau–Rayleigh scenario always overcomes the Rayleigh–Taylor process. The time of the instability development scales as $d_j/u_j \times We^{1/2}$ while the residence time of a fluid particle along the rim is proportional to $d_j/u_j \times We$. Therefore, at a given curvilinear position on the rim, the amplification of the instability will be more important for higher *We*. Assuming that drops start to detach from the sheet when the instability gain reaches a given critical value, we can predict the angle of ejection θ_e of the first drops. That angle should decreases with increasing *We*, or injection velocity u_j. Figure 18(*b*) presents a comparison between the experimental θ_e and that predicted for a critical gain adjusted to 6, 6.5 and 7, respectively, for $2\alpha = 117°$, $88°$ and $72°$. The rim diameter d_b is independent of the jet velocity for a given impact angle, and it sets the time scale of the Plateau–Rayleigh instability ($\sim d_b^{3/2}$). The critical gain is thus kept constant over the whole velocity range. However, the rim size is more and more underestimated by the model as the impact angle decreases (figure 5*a*). As a consequence, a given value of the gain is reached earlier, or for smaller θ, than the measured angle of ejection. The gain has

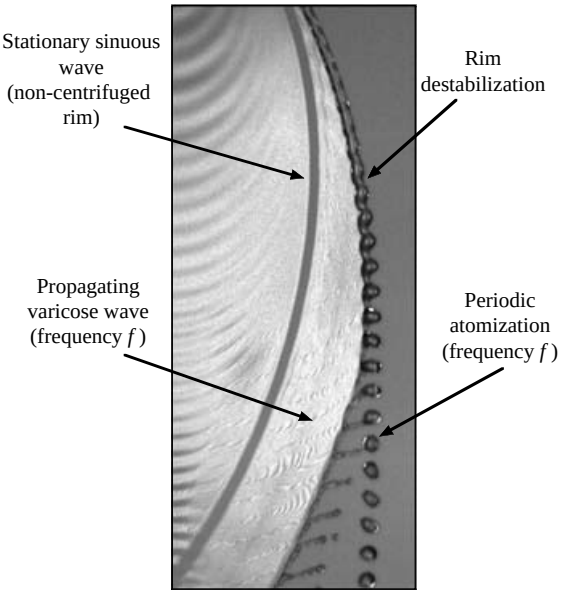

FIGURE 19. Summary of the sheet rim destabilization with all its facets: the sinuous waves propagating from the impingement region, the stationary sinuous wave corresponding to the balance of the sinuous celerity and fluid velocity ('non-centrifuged rim'), the varicose undulations whose frequency matches the frequency of the rim destabilization, and the corresponding unstable ligaments from which drops are produced.

thus to be increased when α decreases in order to fit the experimental data. This artefact of the model explains why the gain has to be adjusted from 6 to 7 when the impact angle is varied from 117° to 72°.

The destabilization of the sheet rim is summarized in figure 19 which displays all the facets of the phenomenon: the sinuous waves propagating from the impingement region, the stationary sinuous wave corresponding to the balance of the sinuous celerity and fluid velocity ('non-centrifuged rim'), the varicose undulations whose frequency matches the most unstable frequency of the rim, and the corresponding unstable ligaments from which drops are produced.

6. Fragmentation

For smaller drops to form from a compact liquid volume, the liquid has to take a shape that is unstable under the action of capillary forces, and this selects the thread, or ligament conformation. In the present atomization process, as in the others, the last step before the production of drops is thus the formation of elongated ligaments, as we can see from figure 20.

The overall drop size distribution formed by the destabilization of these ligaments has been characterized from a collection of frozen images of the spray obtained by a $5\,\mu$s flash lamp triggered by a Hamamatsu ORCA 1280×1024 pixels CCD array. The image-processing technique was originally described in Marmottant (2001) and Marmottant & Villermaux (2004*a*, *b*). The diameter d of the in-focus drops is determined from their projected area A by $d = (4A/\pi)^{1/2}$. Blurred overlapping drops and those smaller than 40×40 pixels on the original images are rejected. Only the drops ejected from the rim are taken into account; those resulting from the merging

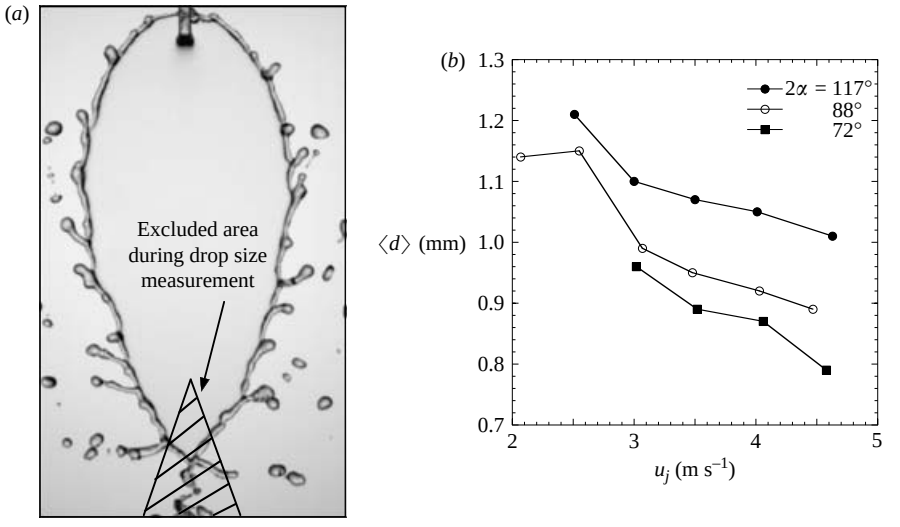

FIGURE 20. (*a*) Fragmented water sheet and definition of the area not taken into account for the drop size measurements. (*b*) Mean drop size $\langle d \rangle$ as a function of the jet velocity for three angles of collision: ●, 117°; ○, 88°; ■, 72°.

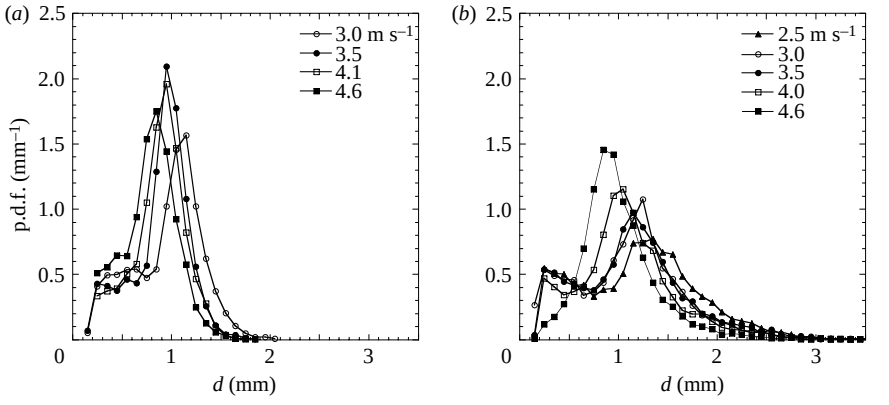

FIGURE 21. (*a*) Probability density functions of the drop size d for several jet velocities, (*a*) $2\alpha = 72°$, (*b*) $2\alpha = 117°$.

of the two rims at the bottom of the sheet were excluded, as sketched on figure 20(*a*). Of the order of 1500 to 5000 drops were processed for each collision condition. These include, in this high-Reynolds-number limit, two control parameters, that is the liquid jet velocity, or injection Weber number We, and the collision angle 2α. The jet diameter d_j is set to 1.05 mm.

Figure 21 presents the probability density functions (p.d.f.) of the drop diameter d for several jet velocities and two collision angles 2α, 72° and 117°. The distributions are positively skewed, and present a principal peak near 1 mm and a smaller one near 0.25 mm. The drastic fall below sizes of the order of 0.1 mm is an artefact of the image-processing technique. The location of the peak moves towards smaller sizes, and the large excursion wing of the distribution relaxes towards zero faster when the jet velocity increases at a fixed angle. The drop size distribution becomes broader for high collision angle at a fixed velocity. Typical snapshots are shown in

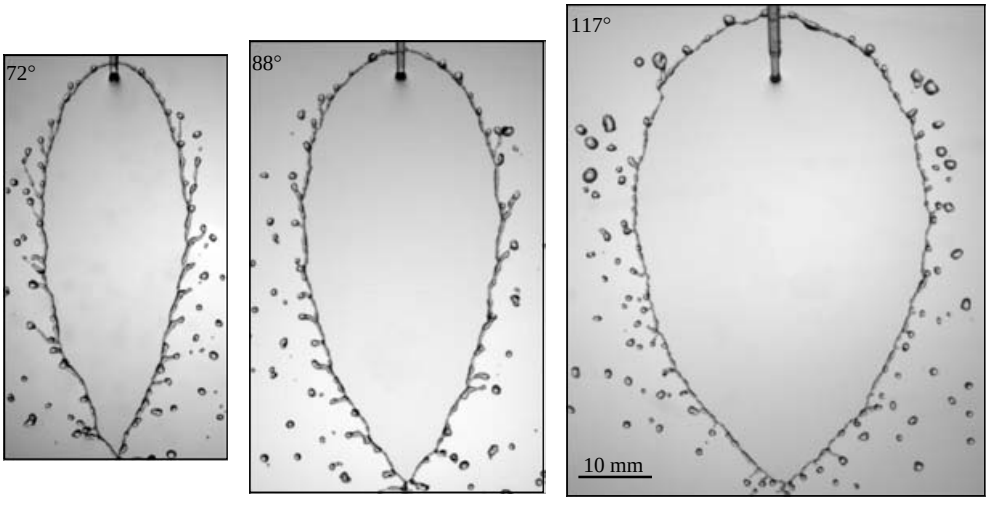

FIGURE 22. Water sheet fragmentation for three collision angles, the jet velocity is equal to $4\,\mathrm{m\,s^{-1}}$ and the jet diameter is 1.05 mm. The elongation of the ligaments is clearly enhanced when the collision angle is decreased.

figure 22 for three collision angles and for the same jet velocity; it is seen that the ligaments mediating the drop formation become more elongated when α decreases. They also become thinner when the velocity increases. These trends are visible on the dependencies of the arithmetic mean drop size $\langle d \rangle$ as a function of jet velocity and collision angle, as shown in figure 20(*b*). In what follows, the brackets stand for the average over the size distribution. For instance $\langle d^q \rangle$, where q is any real number, stands for

$$\langle d^q \rangle = \int d^q P(d)\,\mathrm{d}d \quad \text{with} \quad \int P(d)\,\mathrm{d}d = 1. \tag{6.1}$$

The mean drop size decreases slowly with the jet velocity and becomes larger when the angle of collision increases.

Each ligament carries away a volume of liquid V equal to the sum of the volumes of all the drops issuing from it after breakup. This volume defines the diameter d_0 of the sphere containing all the drops as $d_0 = (6V/\pi)^{1/3}$. The equivalent sphere diameter d_0 is itself distributed from one ligament to another for given operating conditions. Its average value $\langle d_0 \rangle$ is roughly 2.5 times larger than the corresponding average drop size for the same conditions (figure 23), so that the volume V is on average about 15 times larger than the average volume of one drop. Figure 24 shows the probability density function P_L of d_0 normalized by its arithmetic mean $\langle d_0 \rangle$, superimposed on the overall drop size distribution in the spray for the same conditions.

Two collision angles 2α are considered, 72° and 117°. The number of ligaments processed is 184 for $2\alpha = 72^\circ$ and 163 for $2\alpha = 117^\circ$. In each case, the distribution of the ligament equivalent sizes d_0 is narrower than the global distribution of the drop sizes. This important fact indicates that the distribution of drop sizes in the spray relies on the distribution of the drops resulting from the ligament breakup process and not on the distribution of the ligament volumes. In other words, the crucial step for understanding the spray structure is the ligament breakup operation. This observation is consistent with that made by Villermaux *et al.* (2004) in a related context.

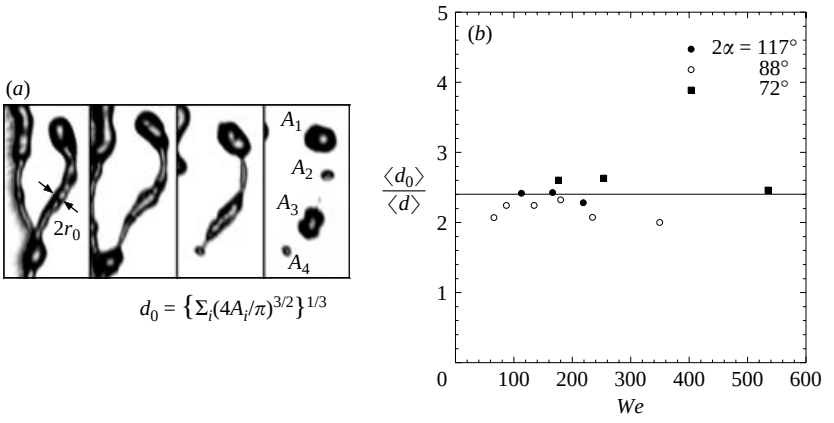

FIGURE 23. (*a*) Definition of the measurement of the equivalent sphere diameter of a ligament d_0. (*b*) Value of the equivalent sphere diameter normalized by the average drop size for several injection conditions. Typically, $\langle d_0 \rangle / \langle d \rangle \approx 2.5$.

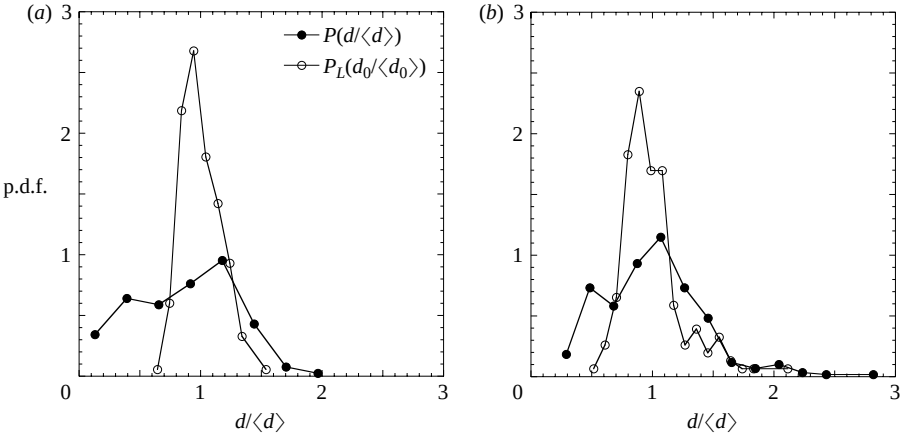

FIGURE 24. (*a*) Probability density functions normalized by ●, the mean size of the drops diameter d and ○, the ligaments size d_0, (*a*) $2\alpha = 72°$, $u_j = 4.2\,\mathrm{m\,s^{-1}}$, (*b*) $2\alpha = 117°$, $u_j = 3.9\,\mathrm{m\,s^{-1}}$.

6.1. *Ligament dynamics and atomization quality*

The capillary destabilization of the rim induces liquid mass concentrations and depletions along the curved rim. The massive regions are preferentially centrifuged while keeping their axial velocity. Because the axial velocity has a positive gradient along the rim, the volume $V \sim d_0^3$ of these massive regions thus elongates and stretches in the form of ligaments, with their foot attached to the rim until they destabilize by capillarity. This process lasts for a period equal to the capillary time scale based on the entrained volume i.e. $\sqrt{\rho V/\sigma}$ (see e.g. Marmottant & Villermaux 2004*a*). A crucial fact is that although this time scale has the same scaling dependence as $t_{PR} = (\rho d_b^3/\sigma)^{1/2}$, it is appreciably larger in absolute value, because $V \approx 20 d_b^3$ is substantially larger than d_b^3. The impact of the longitudinal stretch was negligible on the rim dynamics, but it is significant on that of the detaching ligaments.

The dynamics of the perturbed ligaments can be idealized using the same line of thought as in § 5. We denote by x the longitudinal coordinate of the ligament,

u_0 its axial velocity and r_0 is current radius. Assuming that the stretch γ is uniformly distributed along the ligament, the basic state describing its shape is thus $\{u_0, r_0\} = \{\gamma x, d_0/2\mathrm{e}^{-\gamma t/2}\}$ since $\partial_t r_0/r_0 = -\gamma/2$ by mass conservation in cylindrical coordinates. The stability of this solution is investigated by considering the dynamics of small velocity and radius perturbations u and r which reads

$$\left.\begin{aligned} &\partial_t r + \frac{\gamma}{2} r + \frac{r_0}{2}\partial_x u = 0, \\ &\partial_t u + \gamma u = -\frac{\sigma}{\rho}\left(-\frac{1}{r_0^2}\partial_x r - \partial_x^3 r\right), \end{aligned}\right\} \tag{6.2}$$

leading to an evolution equation for the radius perturbation

$$\partial_t^2 r + 2\gamma\,\partial_t r + \tfrac{3}{4}\gamma^2 r - \frac{\sigma}{2\rho r_0^3}\left(-r_0^2\partial_x^2 r - r_0^4\partial_x^4 r\right) = 0, \tag{6.3}$$

which describes the dynamics of the radius modulations along the ligament. This is again the characteristic equation of an over-damped oscillator because of the stretching term, with a source term depending on the shape of the radius undulations via its spatial derivatives through the Laplace pressure. The radius of the basic state is itself time-dependent as $r_0(t) = d_0/2\mathrm{e}^{-\gamma t/2}$. We thus rescale time by $\sqrt{2\rho r_0(0)^3/\sigma}$, wavenumbers by $r_0(0) = d_0/2$, and look for solutions of the form $r = \xi(t)\mathrm{e}^{\mathrm{i}kx}$ to obtain

$$\partial_t^2\xi + 2\gamma\,\partial_t\xi + \tfrac{3}{4}\gamma^2\xi - (k^2 - k^4 e^{-3\gamma t})\mathrm{e}^{-3\gamma t/2}\xi = 0. \tag{6.4}$$

For the reason explained in § 5, material fluid particles are stretched by the base flow, and so are the radius modulations. Equation (6.4) incorporates this effect through the stretching of the wavenumbers where an initial k becomes $k\mathrm{e}^{-\gamma t}$ over time. For a wavenumber k lying in the initial unstable range ($k < 1$), the early time ($\gamma t \ll 1$) unstable branch for ξ is proportional to $\exp(-\gamma + \sqrt{\gamma^2/4 + k^2 - k^4})t$ and actually leads to an amplification, provided the stretching rate is not too strong, that is, for the initially most amplified mode $k_m = 1/\sqrt{2}$ when $\gamma < 1/\sqrt{3}$. This phenomenology is in qualitative agreement with Frankel & Weihs (1985). The long time ($\gamma t \gg 1$) form of ξ is always dominated by the stretching which decays as $\mathrm{e}^{-\gamma t/2}$, thereby following the stretching-induced rate of approach of the marginal stability condition at $k = 0$, which itself follows the thinning rate of the base ligament radius $r_0 \sim \mathrm{e}^{-\gamma t/2}$.

Figure 25 summarizes the properties of this simple model. Its interest is to provide a prediction for the maximal amplitude of the radius modulations ξ relative to the base radius r_0. This information is of prime importance since the ratio of these two quantities determines the fate of the ligament rupture, and specifically the polydispersity of its fragments. Indeed, analysing the longitudinal rearrangements of the fluid particles constitutive of a free ligament, Villermaux *et al.* (2004) have concluded that the modulation amplitudes of its radius are likely to undergo a random addition process selecting the particular family of the gamma distribution functions. In this vision, these modulations, and their associated distribution, ultimately set the distribution of the drop sizes d after ligament breakup, which is

$$p(X) = \frac{n^n}{\Gamma(n)} X^{n-1}\mathrm{e}^{-nX} \quad \text{where} \quad X = \frac{d}{\langle d\rangle}. \tag{6.5}$$

The shape of the experimental drop size distributions is well represented by (6.5) for various collision angles and Weber numbers once the order n is properly adjusted, as seen in figure 26. The parameter n reflects the regularity of the initial shape of the

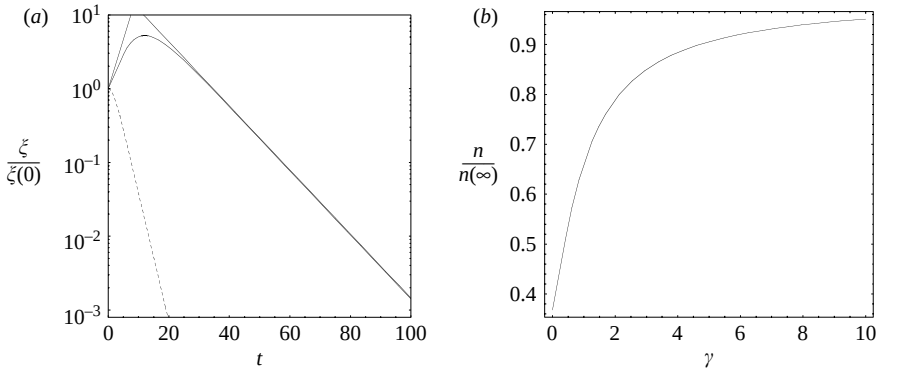

FIGURE 25. (*a*) Temporal evolution of the amplitude $\xi(t)/\xi(0)$ according to (6.4) for $\gamma = 0.2$ (weak stretching, continuous line) and $\gamma = 0.8$ (strong stretching, dashed line), with $k = 1/\sqrt{2}$. The straight lines are the short-time growth, and long-time relaxation limit behaviours for $\gamma = 0.2$. (*b*) Ratio of the order n to its maximal value $n(\infty) = (r_0/\xi)^2_{t=0}$ given by (6.6).

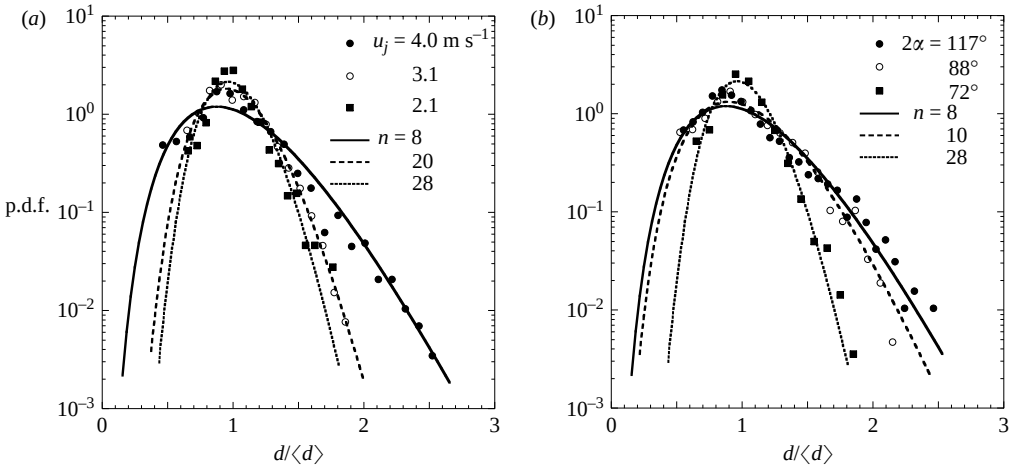

FIGURE 26. Probability density functions of the drop sizes normalized by the mean drop size $d/\langle d\rangle$ for: (*a*) a fixed collision angle $2\alpha = 88°$ and three impacting velocities; (*b*) a fixed impacting velocity $u_j = 3.5\,\mathrm{m\,s^{-1}}$ and three collision angles. The fitted curves are gamma distributions with the parameter n as indicated in each case.

ligament, its relative roughness in some sense since it is given by

$$n = \frac{1}{\zeta - 1} \quad \text{with} \quad \zeta = \frac{\langle r^2\rangle}{\langle r\rangle^2}, \tag{6.6}$$

the averages in computing ζ being taken along the ligament so that $\langle r^2\rangle = r_0(t)^2 + \xi(t)^2$ and $\langle r\rangle^2 = r_0(t)^2$ at any time t. The parameter ζ represents the ratio of the second moment of the radius distribution along the ligament to the square of its mean, and was introduced by Villermaux *et al.* (2004) as the parameter setting the ultimate drop size distribution after breakup. A smooth thread has $\zeta \approx 1$ and thus a very large n giving rise to a close to uniform distribution of drop sizes since $p(X) \xrightarrow{n\to\infty} \delta(X-1)$, whereas a corrugated ligament with $\zeta > 1$ induces a skewed broader distribution of sizes with an exponential tail.

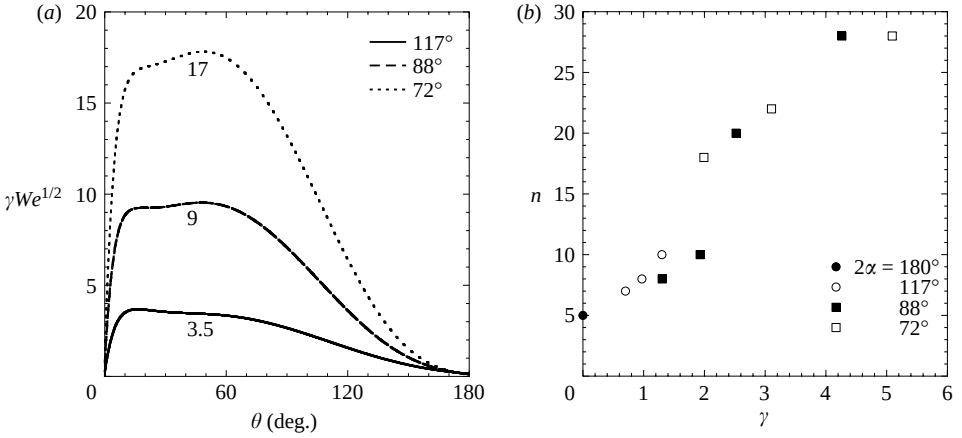

FIGURE 27. (*a*) Non-dimensionalized stretching rate γ multiplied by $We^{1/2}$ versus the angular position θ for three collision angles. (*b*) Experimental parameter n of the gamma distributions versus γ for all the collision conditions investigated.

The above instability analysis gives a status to n, therefore making the connection between elementary fluid mechanics and global statistics possible. Indeed, the ligament is stretched as long as it is pulled by its foot attached to the rim and this lasts for a period given by the capillary time based on its initial size; the stretching period thus lasts up to $t = O(1)$ in the dimensionless units of the stability analysis, providing

$$n \sim \left.\frac{r_0^2}{\xi^2}\right|_{t=1} = \left.\frac{r_0^2}{\xi^2}\right|_{t=0} \exp(\gamma - \sqrt{\gamma^2+1}). \tag{6.7}$$

The transient development of the capillary instability at the early stages of its elongation sets the corrugations of the ligament's radius at the moment it detaches. These corrugations are more pronounced when the stretching is weak, hence giving a lower value of n characteristic of broad distributions of drop sizes. If the stretch is strong, the ligament is smoother with a large n giving a narrower distribution.

As discussed before (5.6), the stretching rate γ decreases when We increases, simply because the sheet becomes larger. It is then expected that n becomes smaller for increasing injection velocity, consistent with the trend visible in figure 26(*a*). The study of the basic state in § 3 has also shown that, for a fixed injection velocity, the stretching rate increases with decreasing collision angle 2α (see e.g. figures 5 and 27(*a*)). It is thus expected that n becomes smaller for increasing collision angle, a trend also consistent with figure 26(*b*).

When plotted versus the stretching rate γ in figure 27(*b*), the values of n for all the impacting conditions fall nicely on a master curve of the form expected from (6.7). Another prediction of the present vision concerns the saturation of n at large γ: the stretch at most suppresses the growth of the capillary instability along the ligament, but not the amplitude of the initial corrugations seen at the scale of the current ligament radius; this is a consequence of the linearity of our theory. As is clear from (6.7) and figure 25, the order of the gamma distributions n saturates at large stretching rate γ, here at about $n(\infty) = (r_0(0)/\xi(0))^2 \approx 30$: although its corrugations diminish in absolute amplitude, a ligament, even strongly stretched, cannot be smoother, relative to its current thickness, than it was initially, as is evident geometrically. This expected saturation is not inconsistent with the measurements reported in figure 27(*b*).

6.2. *Viscous slowing*

Except for the initial perturbation state of the impacting jets, for which the more viscous experiments using ethanol gave rise to more stable sheets compared to water experiments, we have not invoked viscous effects. Our description of both the rim destabilization, and that of the ligament dynamics, is inviscid.

It is not difficult, however, to account for liquid viscosity and to estimate the amplitude of its impact on the dynamics. In the slender-slope approximation, the equation of motion for the axial velocity u in (5.1) or (6.2) incorporates an additional viscous term given by $(3\nu/r^2)\partial_x(r^2\partial_x u)$ discovered by Trouton (the factor 3 in particular, see Trouton 1906). Accounting for this ingredient in, for instance, the ligament dynamics, (6.3) becomes

$$\partial_t^2 r + 2\gamma\,\partial_t r + \tfrac{3}{4}\gamma^2 r - \frac{\sigma}{2\rho r_0^3}\left(-r_0^2\partial_x^2 r - r_0^4\partial_x^4 r\right) - 3\nu\left(\partial_{xxt}^3 r + \tfrac{1}{2}\gamma\,\partial_x^2 r\right) = 0. \tag{6.8}$$

The magnitude of the ratio of the viscous, slowing-down term to the capillary term is initially of order

$$\frac{3\nu}{r_0(0)^2}\sqrt{\frac{2\rho r_0(0)^3}{\sigma}} \sim \sqrt{\frac{\rho\nu^2}{\sigma r_0(0)}} = \frac{1}{Re}, \tag{6.9}$$

which, with $r_0(0) \approx 1\,\mathrm{mm}$, gives $Re \approx 100$ for water, thus supporting the inviscid description. If Re is larger than unity, it is nevertheless close to the border below which viscosity slows down the capillary breakup by increasing t_{PR} (Eggers 1997). In the viscous limit, ligaments are stretched longer, and are therefore thinner at breakup, producing smaller drop sizes, and also narrower distributions (see e.g. Marmottant & Villermaux 2004*b*). This can be seen qualitatively on some pictures of Bush & Hasha (2004) who used liquids up to 50 times more viscous than water.

7. Conclusion

The interest of the jets colliding at an angle configuration for the atomization problem is that the quality of atomization, namely the distribution of the drop sizes, can be manipulated from the experimental parameters. Resulting from an equilibrium of the fluid inertia and surface tension, the size of the liquid sheet formed from the jet impact scales as $d_j We$ where d_j is the jet diameter, and We the injection Weber number. Less trivial is the detailed shape and thickness distribution of the sheet, and the diameter and velocity of the liquid in the rim bordering the sheet. These quantities are described by an appropriate formulation of mass and momentum balances along the sheet rim. An important peculiarity of this system is that the axial velocity in the rim suffers an axial stretch whose magnitude increases when the collision angle decreases (§ 3).

The destabilization of the rim, either triggered artificially by an external perturbation, or naturally via the disturbances injected by the jets themselves in the sheet, reveals that the instability is of a capillary type, selecting a wavelength proportional to the rim diameter. The onset and amplification of this instability is very sensitive to the thickness perturbations injected in the sheet by the colliding conditions (§§ 4 and 5).

The capillary destabilization of the rim induces liquid mass concentrations and depletions along the curved rim. The massive regions are preferentially centrifuged while keeping their axial velocity. Because the axial velocity has a positive gradient along the rim, the volume of these massive regions elongates and stretches in the

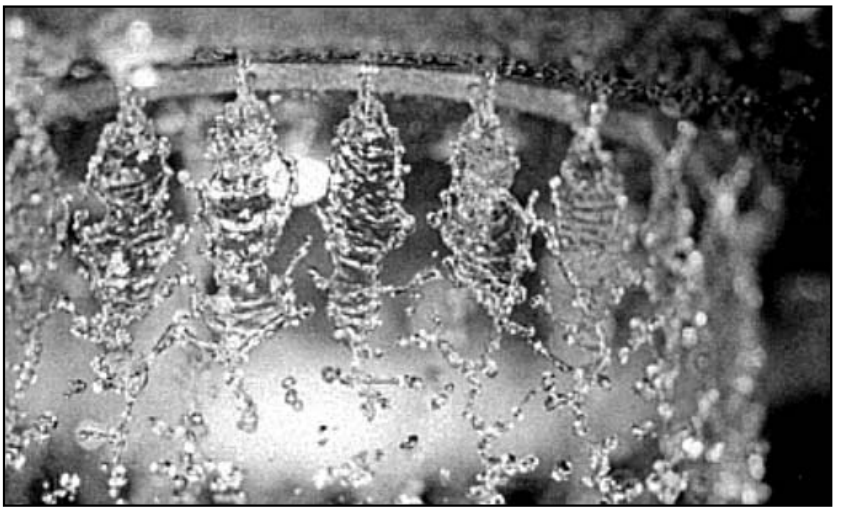

FIGURE 28. Impacting jets in the combustion chamber of the gas generator of an industrial propulsion engine. Courtesy J.-L. Thomas, SNECMA.

form of ligaments, with their foot attached to the rim until they destabilize by capillarity. The transient development of the capillary instability at the early stages of a ligament elongation sets the corrugations of its section at the moment it detaches. These corrugations are more pronounced when the stretching is weak, hence giving a broader drop-size distribution. If the stretch is strong, the ligament is smoother, giving a narrower distribution. The size distributions pertain to the gamma family and are parameterized by the single quantity γ, the rate of stretch in the rim normalized by a capillary time scale, and depends both on the Weber number, and the collision angle (§ 6).

These heuristic findings have a natural extension in the context of liquid propulsion in closed combustion chambers where impacting jets are frequently used (Yang & Anderson 1995). Figure 28 illustrates such a real-world set-up.

It has been known for a long time in this particular activity that a combustion instability may occur, linked to the injection parameters of the propellants. The instability results in a global coupling between the pressure oscillations in the combustion chamber and the atomization of the propellants. The oscillation has a most 'dangerous mode' with a frequency of the order of the injection frequency u_j/d_j (Anderson *et al.* 1995). The present work provides a mechanistic explanation of this fact: the sheet rim diameter is of the order of the jet diameter d_j (§ 3) and is linearly unstable via a capillary instability whose preferred wavelength is of the order of d_j (§ 5). This 'fragile object' is therefore an amplifier of perturbations when those have the appropriate spatial wavelength (§ 4). These are precisely generated by turbulent jets which inject modulations of thickness and velocity in the sheet with a spatial wavelength given by that of the preferred jet mode, that is d_j (Dombrowski & Hooper 1963). The colliding jets configuration is therefore a self-excited system which produces a segregation of the reactants in the combustion chamber at the rim destabilization frequency, namely u_j/d_j (Heidmann *et al.* 1957). It sometimes results in a catastrophic feedback with the internal pressure fluctuations in the chamber which in turn modulate the injection rate in the jets themselves (Miesse 1955; Meier,

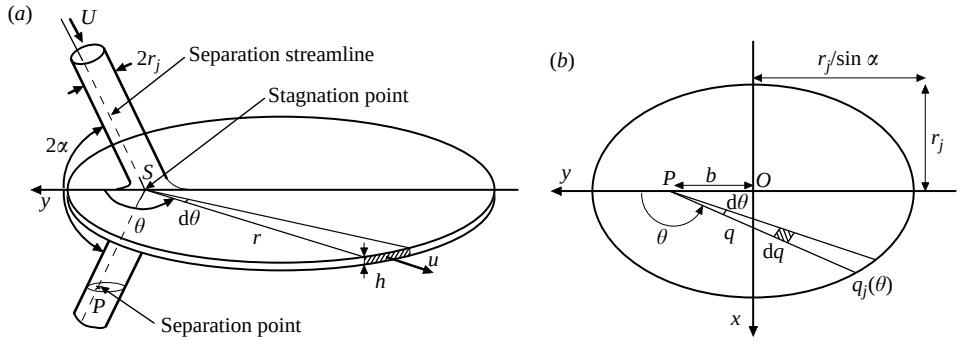

FIGURE 29. (*a*) Coordinates of the jet impact system. (*b*) Cross-section of an incident jet parallel to the sheet plane.

Klopper & Grabitz 1992), possibly leading to the extinction of the combustion, or to damage of the chamber.

This work was supported by CNES under contract 02-0485-00. We acknowledge J.-L. Thomas, from SNECMA, for providing us with figure 28 and C. Clanet for discussions.

Appendix A. Sheet speed and thickness distributions for incident jets with a parabolic velocity profile

The interferometry sheet thickness measurements by Shen & Poulikakos (1998) and Choo & Kang (2001) indicate a deviation from the hypothesis of Hasson & Peck (1964), namely that of a flat uniform velocity profile of the incident jets. Choo & Kang (2002) have shown the existence of a velocity distribution in the sheet which is inherent in the initial jet velocity profile. In this Appendix, we determine the sheet velocity $u(\theta, \alpha)$ and thickness $h(r, \theta, \alpha)$ distributions by taking into account the existence of a velocity profile U in the incident jets. A sketch of the jet impact introducing the coordinates and the sheet parameters is given in figure 29(*a*). We assume that a Poiseuille flow has been established in the injectors, and we keep it unaltered up to the merging point of the jets. Obviously, the velocity profile relaxes by vorticity diffusion downstream of the injector exit, but we assume that it does so for a time lapse long enough to keep the parabolic profile essentially unaltered; the relaxation occurs from the free gas/liquid interface, and the penetration depth of the relaxed profile is of the order of $\delta \sim \sqrt{\nu t}$. If the two jets are initially separated by a distance of the order of d_j, the time offered for the relaxation is of order d_j/u_j so that $\delta/d_j \sim Re^{-1/2}$. This assumption is thus all the more valid when the Reynolds number is high. In any event, this 'unaltered' parabolic profile is a limit worth investigating as a complement to Hasson & Peck (1964). As for the velocity across the sheet itself u, following the same argument, very rapidly becomes uniform owing to the strong decrease of the thickness h with distance from the impact point.

The radial flow in the sheet can be represented by a source with an origin located at the stagnation point S (figure 29*a*). The jet streamlines are initially parallel and one of them, the separation streamline, reaches the stagnation point S. Mass, energy and

momentum fluxes through an angular element of the jet taken in the plane parallel to the sheet and relative to the separation streamline are equal to the fluxes through a vertical section of the sheet at a distance r from S. The section of the jet parallel to the sheet plane is shown on figure 29(b). This is an ellipse with a major axis equal to $2r_j/\sin\alpha$ and a minor axis equal to $2r_j$, where r_j is the radius of the incident jets. The separation streamline crosses this ellipse at the separation point P which is taken as the origin of the cylindrical coordinate system $\{q, \theta\}$. The distance between P and the centre of the jet O is equal to b. Using r_j as the length scale and r_j/u_j as time scale, the Poiseuille dimensionless parabolic velocity profile U of the jets, in this system of reference, is

$$U = 2(1 - (q\cos\theta + b)^2 \sin^2\alpha - q^2\sin^2\theta). \tag{A 1}$$

The mass flux conservation through a section of angular aperture equal to $\mathrm{d}\theta$ is

$$u(\theta,\alpha)h(r,\theta,\alpha)r\,\mathrm{d}\theta = 2\int_0^{q_j} U\sin\alpha q\,\mathrm{d}\theta\,\mathrm{d}q, \tag{A 2}$$

where q_j is the location of the jet interface which is deduced from the polar equation of the ellipse

$$(q\sin\theta)^2 + (q\cos\theta + b)^2\sin^2\alpha = 1, \tag{A 3}$$

and is equal to

$$q_j = \frac{-b\cos\theta\sin^2\alpha + (1 - \cos^2\theta\cos^2\alpha - b^2\sin^2\theta\sin^2\alpha)^{1/2}}{1 - \cos^2\theta\cos^2\alpha}. \tag{A 4}$$

For high Weber and small Froude numbers, that is neglecting surface tension and gravity in the incident fluxes, the conservation of the energy flux is

$$u^3(\theta,\alpha)h(r,\theta,\alpha)r\,\mathrm{d}\theta = 2\int_0^{q_j} U^3\sin\alpha q\,\mathrm{d}\theta\,\mathrm{d}q. \tag{A 5}$$

Using the velocity profile given by equation (A 1), the integrals in equations (A 2) and (A 5) are

$$\int_0^{q_j} Uq\,\mathrm{d}q = (1 - b^2\sin^2\alpha)q^2 - \tfrac{4}{3}b\cos\theta\sin^2\alpha q^3 - \tfrac{1}{2}(\cos^2\theta\sin^2\alpha + \sin^2\theta)q^4 \tag{A 6}$$

and

$$\begin{aligned}
\int_0^{q_j} U^3 q\,\mathrm{d}q &= 4(1 - b^2\sin^2\alpha)^3 q_j^2 - 16(1 - b^2\sin^2\alpha)^2 b\cos\theta\sin^2\alpha q_j^3 \\
&\quad + 2\{(1 - b^2\sin^2\alpha)(-2(1 - b^2\sin^2\alpha)(1 - \cos^2\theta\cos^2\alpha) \\
&\quad + 4b^2\cos^2\theta\sin^4\alpha) + 8b^2\cos^2\theta\sin^4\alpha(1 - b^2\sin^2\alpha) - (1 - \cos^2\theta\cos^2\alpha) \\
&\quad \times (1 - b^2\sin^2\alpha)^2\}q_j^4 + \tfrac{8}{5}\{8(1 - b^2\sin^2\alpha)b\cos\theta\sin^2\alpha(1 - \cos^2\theta\cos^2\alpha) \\
&\quad - 2b\cos\theta\sin^2\alpha(-2(1 - b^2\sin^2\alpha)(1 - \cos^2\theta\cos^2\alpha) + 4b^2\cos^2\theta\sin^4\alpha)\}q_j^5 \\
&\quad + \tfrac{4}{3}\{(1 - b^2\sin^2\alpha)(1 - \cos^2\theta\cos^2\alpha)^2 - 8b^2\cos^2\theta\sin^4\alpha(1 - \cos^2\theta\cos^2\alpha) \\
&\quad + (1 - \cos^2\theta\cos^2\alpha)(2(1 - b^2\sin^2\alpha)(1 - \cos^2\theta\cos^2\alpha) - 4b^2\cos^2\theta\sin^4\alpha)\}q_j^6 \\
&\quad - \tfrac{48}{7}b\cos\theta\sin^2\alpha(1 - \cos^2\theta\cos^2\alpha)^2\, q_j^7 - (1 - \cos^2\theta\cos^2\alpha)^3 q_j^8.
\end{aligned} \tag{A 7}$$

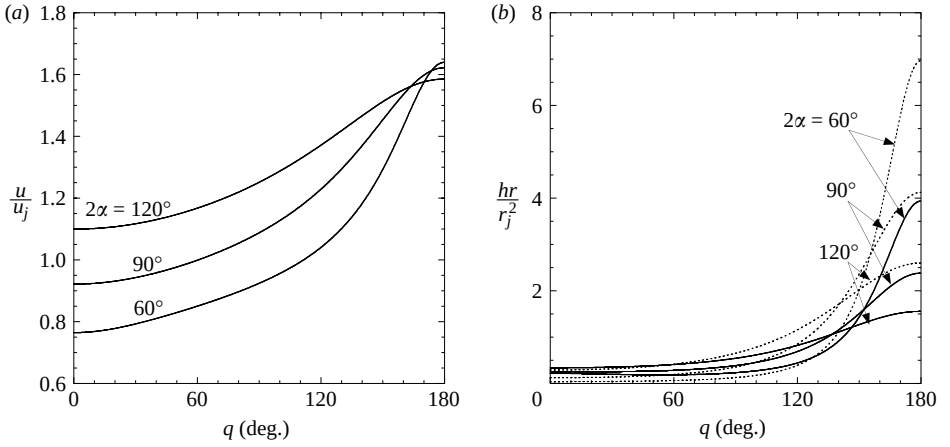

FIGURE 30. (*a*) Polar distribution of the sheet velocity. (*b*) Polar distributions of the sheet thickness derived from a parabolic profile of the incident jets (continuous line) and from an uniform profile (dotted line) (Hasson & Peck 1964).

The sheet features $u(\theta, \alpha)$ and $h(r, \theta, \alpha)$ are then deduced from equations (A 2) and (A 5) using (A 6) and (A 7). They depend on b, the location of the separation point P and therefore that of the stagnation point S. This position is deduced from the conservation of momentum along the y-direction which is written as

$$\int_0^{2\pi} u^2(\theta, \alpha) h(r, \theta, \alpha) r \cos\theta \, \mathrm{d}\theta = -\tfrac{8}{3}\pi \cos\alpha. \tag{A 8}$$

The analytical solution of equation (A 8) has not been determined, but b is found to be equal to $0.68/\tan\alpha$ after numerical integration of (A 8), as shown in figure 31(*a*). The sheet velocity u is plotted in figure 30(*a*) as a function of θ for three impact angles. As measured by Choo & Kang (2002), the maximum velocity lies along the direction of the jets ($\theta = 180°$). The velocity difference between the backwards ($\theta = 0°$) and the forwards ($\theta = 180°$) directions increases as the angle of collision decreases. The polar distribution of the sheet thickness is presented in figure 30(*b*) and is compared with the expression derived by Hasson & Peck (1964). As observed by Shen & Poulikakos (1998) and by Choo & Kang (2001), the sheet is thinner for high azimuthal angles than expected from the prediction of Hasson & Peck.

The contours of the sheet deduced from these new velocity and thickness fields are plotted in figure 31(*b*) for $2\alpha = 89°$ and compared with the experimental shape as well as those derived from the Hasson & Peck correlation. The proposed derivation over-predicts the size of the sheet.

In real situations, the profile is neither purely parabolic, nor purely uniform and the sheet shape lies between both extremes shown on figure 31(*b*). We can now understand the important role played by the initial jet velocity profile on the sheet behaviour; fluctuations of the injection conditions induce non-stationary sheet velocity and thickness fields which trigger the destabilization and the rim towards its fragmentation. This has been observed for the water case (§ 4.2) where perturbations are already present in the jets, and for the ethanol case for which controlled perturbations have been introduced (§ 4.1) and shown to dramatically interfere with the rim dynamics.

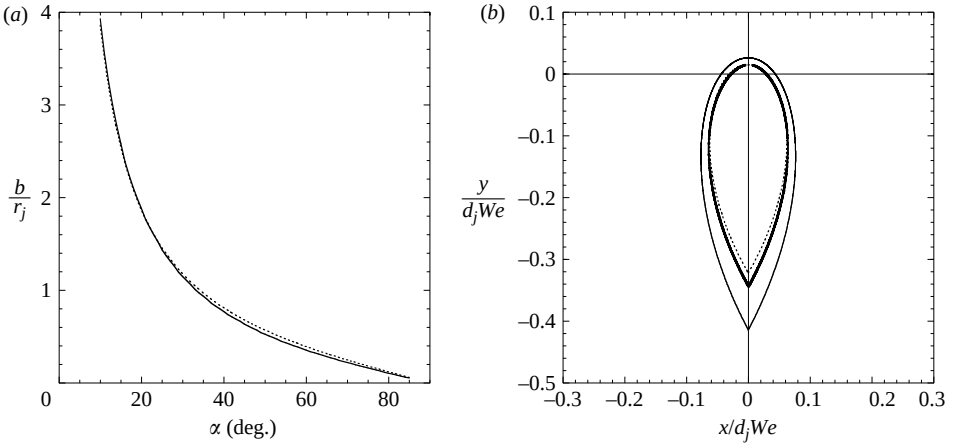

FIGURE 31. (*a*) Distance b between the centreline of the jet and the stagnation point as a function of the impact angle α (continuous line). The dotted line corresponds to $0.68/\tan\alpha$. (*b*) Contours of a liquid sheet formed by the impact at $2\alpha = 89^\circ$ of two jets with a parabolic velocity profile (thin continuous line) compared with the experimental shape (thick continuous line) and using the correlation of Hasson & Peck (1964) (dotted line).

REFERENCES

ANDERSON, W. E., RYAN, H. M. & SANTORO, R. J. 1995 Impinging jet injector atomization. In *Liquid Rocket Engine Combustion Instability*, vol. 169. AIAA.

BAYVEL, L. & ORZECHOWSKI, Z. 1993 *Liquid Atomization*. Taylor & Francis.

BREMOND, N. 2003 Stabilité et atomisation des nappes liquides. PhD thesis, Université de Provence, Marseille.

BUSH, J. W. M. & HASHA, A. E. 2004 On the collision of laminar jets: fluid chains and fishbones. *J. Fluid Mech.* **511**, 285–310.

CHOO, Y. J. & KANG, B. S. 2001 Parametric study on impinging-jet liquid sheet thickness distribution using an interferometric method. *Exps. Fluids* **31**, 56–62.

CHOO, Y. J. & KANG, B. S. 2002 The velocity distribution of the liquid sheet formed by two low-speed impinging jets. *Phys. Fluids* **14**, 622–627.

CLANET, C. & VILLERMAUX, E. 2002 Life of a smooth liquid sheet. *J. Fluid Mech.* **462**, 307–340.

CLARK, D. J. & DOMBROWSKI, N. 1972 On the formation of drops from the rims of fan spray sheets. *J. Aerosol Sci.* **3**, 173–183.

CULICK, F. E. C. 1960 Comments on a ruptured soap film. *J. Appl. Phys.* **31**, 1128.

DOMBROWSKI, N., HASSON, D. & WARD, D. E. 1960 Some aspects of liquid through fan spray nozzles. *Chem. Engng Sci.* **12**, 35–50.

DOMBROWSKI, N. & HOOPER, P. C. 1963 A study of the sprays formed by impinging jets in laminar and turbulent flow. *J. Fluid Mech.* **18**, 392–400.

DOMBROWSKI, N. & NEALE, N. D. 1974 Formation of streams of uniform drops from fan spray pressure nozzles. *J. Aerosol Sci.* **5**, 551–555.

EGGERS, J. 1997 Nonlinear dynamics and breakup of free-surface flows. *Rev. Mod. Phys.* **69**, 865–929.

EGGERS, J. 2002 Dynamics of liquid nanojets. *Phys. Rev. Lett.* **89**, 084502.

EINSENKLAM, P. 1964 On ligament formation from spinning disks and cups. *Chem. Engng Sci.* **19**, 693–694.

FRANKEL, I. & WEIHS, D. 1985 Stability of a capillary jet with linearly increasing axial velocity (with application to shaped charge). *J. Fluid Mech.* **155**, 289–307.

Hasson, D. & Peck, R. E. 1964 Thickness distribution in a sheet formed by impinging jets. *AIChE J.* **10**, 752–754.

Heidmann, M. F., Priem, R. J. & Humphrey, J. C. 1957 A study of sprays formed by two impacting jets. *NACA IN* 3835.

Hinze, J. O. & Milborn, H. 1955 Atomization of liquid by means of a rotating cup. *Trans. ASME* E: *J. Appl. Mech.* **17**, 145–153.

Ho, C. M. & Huerre, P. 1984 Perturbed free shear layers. *Annu. Rev. Fluid Mech.* **16**, 365–424.

Huang, J. C. P. 1970 The break-up of axisymmetric liquid sheets. *J. Fluid Mech.* **43**, 305–319.

Ibrahim, E. A. & Przekwas, A. 1991 Impinging jets atomization. *Phys. Fluids* A **3**, 2981–2987.

Lefebvre, A. H. 1989 *Atomization and Sprays*. Hemisphere.

Mansour, A. & Chigier, N. 1990 Disintegration of liquid sheets. *Phys. Fluids* A **2**, 706–719.

Mariotte, E. 1686 *Traité du mouvement des eaux et des autres corps fluides*. E. Michallet, Paris.

Marmottant, P. 2001 Atomisation d'un liquide par un courant gazeux. PhD thesis, LEGI Grenoble.

Marmottant, P. & Villermaux, E. 2004*a* Fragmentation of stretched liquid ligaments. *Phys. Fluids* **16**, 2732–2741.

Marmottant, P. & Villermaux, E. 2004*b* On spray formation. *J. Fluid Mech.* **498**, 73–112.

Mason, B. J. 1971 *The Physics of Clouds*. Clarendon.

Meier, G. E. A., Klopper, A. & Grabitz, G. 1992 The influence of kinematic waves on jet break down. *Exps. Fluids* **12**, 173–180.

Miesse, C. C. 1955 The effect of ambient pressure oscillations in the disintegration and dispersion of a liquid jet. *Jet Propulsion*, pp. 525–534.

Miller, K. D. 1960 Distribution of spray from impinging liquid jets. *J. Appl. Phys.* **31**, 1132–1133.

Moseler, M. & Landman, U. 2000 Formation, stability, and breakup of nanojets. *Science* **289**, 1165–1169.

Naber, J. D. & Reitz, R. D. 1988 Modeling engine spray/wall impingement. *SAE Paper* p. 880107.

Plateau, J. 1873 *Statique expérimentale et théorique des liquides soumis aux seules forces moléculaires*. Gauthiers Villars, Paris.

Rayleigh, Lord 1879 On the instability of jets. *Proc. Lond. Math. Soc.* **4**, 10.

Rayleigh, Lord 1883 Investigation of the character of the equilibrium of an incompressible heavy fluid of variable density. *Proc. R. Soc. Lond.* **14**, 170–177.

Ryan, H. M., Anderson, W. E., Pal, S. & Santoro, R. J. 1995 Atomization characteristics of impinging liquid jets. *J. Prop. Power* **11**, 135–145.

Saffman, P. G. 1974 The structure and decay of trailing vortices. *Arch. Mech.* **26**, 423–439.

Savart, F. 1833*a* Mémoire sur la constitution des veines liquides lancées par des orifices circulaires en mince paroi. *Ann. chim.* **53**, 337–398.

Savart, F. 1833*b* Mémoire sur le choc de deux veines liquides animées de mouvements directement opposés. *Ann. chim.* **55**, 257–310.

Savart, F. 1833*c* Mémoire sur le choc d'une veine liquide lancée sur un plan circulaire. *Ann. chim.* **54**, 56–87.

Savart, F. 1833*d* Suite du mémoire sur le choc d'une veine liquide lancée sur un plan circulaire. *Ann. chim.* **54**, 113–145.

Seinfeld, J. H. & Pandis, S. N. 1998 *Atmospheric Chemistry and Physics*. John Wiley.

Shen, Y. B. & Poulikakos, D. 1998 Thickness variation of liquid sheet formed by two impinging jets using holographic interferometry. *J. Fluids Engng* **120**, 482–487.

Squire, H. B. 1953 Investigation of the stability of a moving liquid film. *Brit. J. Appl. Phys.* **4**, 167–169.

Taylor, G. I. 1950 The instability of liquid surfaces when accelerated in a direction perpendicular to their plane.i. *Proc. R. Soc. Lond.* A **201**, 192–196.

Taylor, G. I. 1959*a* The dynamics of thin sheets of fluid ii. waves on fluid sheets. *Proc. R. Soc. Lond.* **253**, 296–312.

Taylor, G. I. 1959*b* The dynamics of thin sheets of fluid iii. disintegration of fluid sheets. *Proc. R. Soc. Lond.* **253**, 313–321.

Taylor, G. I. 1960 Formation of thin flat sheets of water. *Proc. R. Soc. Lond.* **259**, 1–17.

Trouton, F. T. 1906 On the coefficient of viscous traction and its relation to that of viscosity. *Proc. R. Soc. Lond.* **77**, 426–440.

Villermaux, E. & Clanet, C. 2002 Life of a flapping liquid sheet. *J. Fluid Mech.* **462**, 341–363.

Villermaux, E., Marmottant, P. & Duplat, J. 2004 Ligament-mediated spray formation. *Phys. Rev. Lett.* **92**, 074501.

Weber, C. 1931 Zum zerfall eines flüssigkeitsstrahles. *Z. Angew. Math. Mech.* **2**, 136.

Yang, V. & Anderson, W. 1995 *Liquid Rocket Engine Combustion Instability*, vol. 169. AIAA.

Yarin, A. L. 1993 *Free Liquid Jets and Films: Hydrodynamics and Rheology*. Longman.